THESIS FOR THE DEGREE OF LICENTIATE OF ENGINEERING

Performance evaluation of battery-based energy storages for various duties

Meryem Ahouad

Department of Electrical Engineering
Chalmers University of Technology
Gothenburg, Sweden, 2026

Performance evaluation of battery-based energy storages for various duties

Meryem Ahouad

Acknowledgements, dedications, and similar personal statements in this thesis, reflect the author's own views.

Department of Electrical Engineering
Chalmers University of Technology
SE-412 96 Gothenburg, Sweden
Phone: +46 (0)31 772 1000

Printed by Chalmers Digital Printing
Gothenburg, Sweden, April 2026

Abstract

The growth of renewable energy increases imbalances between generation and demand, raising the need for frequency ancillary services. Battery Energy Storage System (BESS) are well suited for these services due to their fast response. However, Frequency Containment Reserve (FCR) operation affects both battery degradation and economic performance, making it important to assess the link between operation, ageing, and market remuneration.

This thesis evaluates the degradation and economic performance of BESS providing FCR services, including Frequency Containment Reserve for Normal operation (FCR-N), upward regulation (FCR-D-up), downward regulation (FCR-D-down), and combined configurations. A dynamic simulation with one-second frequency resolution is developed to model battery operation under realistic conditions, including State Of Charge (SOC) management based on Normal state Energy Management mode (NEM) and Alert state Energy Management mode (AEM). Semi-empirical calendar and cycling ageing models based on experimental data are reformulated to enable continuous degradation estimation, while cycling ageing is quantified using a rainflow counting algorithm.

The results show that degradation depends strongly on the SOC operating range. FCR-D up exhibits the highest capacity loss due to long periods at high SOC, while FCR-N shows higher cycling degradation. In contrast, FCR-D down operates mainly at low SOC and shows the lowest degradation.

The economic analysis shows that combined services improve profitability. FCR-N+D achieves the highest annual net profit (1.10 MSEK) for 1 MWh/MW and shortest payback time 2 years, while stand-alone FCR-D services require 3 years to return the investment. A 50% reduction in remuneration still results in acceptable payback periods.

Keywords: BESS, Frequency Containment Reserve (FCR), Lithium-Ion Batteries, Calendar Ageing, Cycling Degradation, SOC, Rainflow Counting, Equivalent Full Cycles (EFC), Nordic Power System, Techno-Economic Analysis

For Awab, my beloved nephew.

Contents

Acknowledgments

I would like to thank my supervisors, Torbjörn Thiringer and Evelina Wikner, for their support, availability, and encouragement throughout these three years. This work would not have been possible without your guidance and insights. I have always looked forward to our meetings; your perspectives have been both valuable and inspiring.

The financial support from Energimyndigheten, Västra Götalandsregionen, Volvo Group, Volvo Cars, Redox.me, Soltech Energy, and Chalmers University of Technology through the Swedish Energy Storage and Balancing Centre is gratefully acknowledged. I also thank the industrial partners of the Swedish Electricity Storage and Balancing Centre for their interest in this research.

I would like to thank Associate Professor Peiyuan Chen for his availability and for being willing to meet and discuss whenever I had questions or doubts.

Additionally, I am grateful to my colleagues and friends at Chalmers University of Technology for the enjoyable fika, shared lunches, and enriching conversations. These moments brought warmth and laughter, and also gave me the chance to learn about different cultures.

Finally, I want to thank my family and friends for their support and encouragement, my mother and my siblings for their never-ending support throughout my years of study.

Acronyms

aFRR Automatic Frequency Restoration Reserve

AEM Alert state Energy Management mode

BESS Battery Energy Storage System

ECM equivalent Circuit Model

ENTSO-E European Network of Transmission System Operators for Electricity

FCR Frequency Containment Reserve

FCR-D Frequency Containment Reserve for Disturbances

FCR-D-up upward regulation

FCR-D-down downward regulation

FCR-N Frequency Containment Reserve for Normal operation

FFR Fast Frequency Response

LER Limited Energy Reservoir

LFP Lithium Iron Phosphate

mFRR Manual Frequency Restoration Reserve

NEM Normal state Energy Management mode

NPV Net Present Value

RR Replacement Reserve

SEI Solid Electrolyte Interphase

SOC State Of Charge

SOE State Of Energy

TSO Transmission System Operator

V2G Vehicle to grid

CHAPTER 1

Introduction

1.1 Background and Motivation

The transition to a low-carbon energy system increase the role of wind and solar power in the electricity sector[1]. This is especially apparent in Sweden, where installed wind power capacity exceed 17 GW in 2024, and solar capacity is also increasing rapidly around 4.8 GW [2]. While this development is essential for meeting climate goals, it also introduces new challenges. Wind and solar are intermittent resources. Their output naturally varies, and increasing their share in the system makes the power grid more vulnerable to imbalances between electricity supply and demand.

Maintaining power balance between supply and demand is necessary to keep the frequency within normal range. Excessive supply increases frequency, while excessive demand decreases it. If the frequency deviation is large, this may lead to disconnection of loads [3]. Disturbances such as unexpected generator outages or rapid changes in renewable output can cause frequency deviations. With fewer conventional synchronous units connected, the grid has less inherent ability to handle these disturbances, which increase the reliance on procured balancing services.

FCR provide the first response to such imbalances. Traditionally, hydropower and thermal units have delivered most of this capacity. However, as the energy system changes, new technologies capable of fast responses are becoming increasingly important.

Lithium-ion batteries are receiving increasing attention. Due to their rapid response, high efficiency, and flexible operation, they are particularly well suited for FCR applications [4, 5]. In 2026 pack prices drop to be around 108 $/kWh (Fig. 1.1) [6], which allowed several large BESS installations in Sweden and Finland to participate in the FCR market [7].

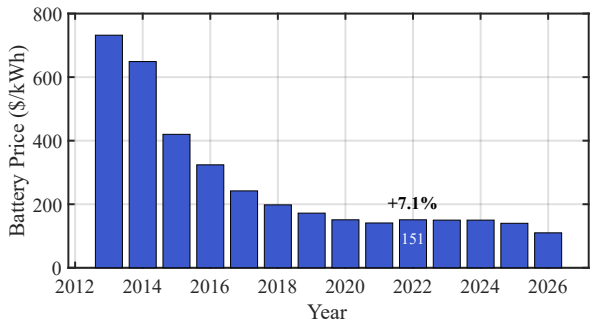

Figure 1.1: Evolution of lithium-ion battery pack prices from 2012 to 2026.

FCR activation involves frequent, micro-cycles (0.1 % to 5 % ΔSOC), combined with long periods at medium or high SOC [8]. These operating conditions can accelerate both cycle and calendar ageing [9], leading over time to reduced usable capacity and increased internal resistance. Since battery replacement typically accounts for 60–70% of total BESS costs [5], understanding how FCR operating affect degradation is important.

In addition, the updated Nordic FCR requirements add more complexity to battery operation by requiring continuous availability for both upward and downward regulation. This increases the need for more precise SOC management, since the battery must remain within a suitable operating window to deliver power in both directions at all times. As a result, many existing degradation models do not fully reflect the conditions that batteries experience during real FCR operation.

These challenges motivate the work presented in this thesis. The battery is operated according to Nordic FCR requirements, and different FCR services

are studied to evaluate their impact on ageing. By comparing degradation for all FCR services and linking it to cost and net profit, this work aims to clarify the relationship between battery degradation, cost, and net profit.

1.2 Previous Studies

Several studies have investigated BESS providing FCR, with a focus on economic performance, operational strategies, and battery degradation. Multiple studies indicate that FCR is one of the most profitable services for BESS in Europe. A comparative assessment of major European electricity markets shows that energy arbitrage alone is generally not economically viable. In contrast, participation in FCR markets can ensure high and stable utilization of battery capacity. For example, FCR-N in Denmark achieved nearly 100% potentially profitable utilization in 2021 [10].

For Sweden, mixed integer linear programming (MILP) models with detailed cycle and calendar ageing indicate that bidding in day ahead market together with FCR-N and Frequency Containment Reserve for Disturbances (FCR-D) up/down can increase profit by a factor of about 22 compared with day ahead only operation [11].

Similarly, Wesselmann et al. analyze single-use and multi-use grid-scale BESS in Germany using a techno-economic simulation. The model evaluates a 20 year project based on return on investment and Net Present Value (NPV). The study compares primary control reserve and enhanced frequency response, both with and without peak shaving. The results show that enhanced frequency response alone is the most profitable service, while combining it with peak shaving can further increase financial returns [12].

Giannakopoulos et al analyse BESS profitability in Greek day ahead market and FCR markets. They confirm that combining day ahead market and FCR give higher profits than either market alone, but results are sensitive to uncertainty in prices and utilisation factors [13].

Focusing more specifically on individual FCR products, a similar case study in the Nordic context report that FCR-D up generally provides the shortest payback times, whereas FCR-N has lower returns for the same BESS [14].

As BESS are limited energy reservoirs, many works also address operational strategies. Under Nordic requirements, Divshali [15] and Evens propose bidding and online control strategy that restore SOC while including a lifetime

model to optimise profit using a 600 kW/300 kWh BESS case study, they report annual revenues of 38 k€ corresponding to a payback period of about 6-8 years.

Several studies analyze the impact of FCR operation on battery ageing. Long-term measurements from a 6 MW/7.5 MWh hybrid system show that FCR keeps the average SOC close to 50%, with low C-rates (0.08C) and mainly shallow charge discharge cycles. After four years of operation, the lithium-ion batteries experienced about 5% capacity loss, while lead-acid batteries lost up to 36%. This result suggests that calendar ageing is the main degradation under FCR operation [16].

Another study on a 7.2 MW/7.12 MWh battery system in the German FCR market applies a semi-empirical model to separate the effects of operating strategy and temperature on degradation. The authors report up to 0.97% difference in annual capacity loss between the coldest and warmest battery packs, indicating that better thermal management could increase battery lifetime by 11 years [17].

Khajeh et al. show that a 50 kWh lithium-ion battery providing FCR-N in Finland earns about 1178€ over three months. However, cycling degradation reduces revenue by approximately 0.06€ per cycle, highlighting the importance of including battery ageing in economic assessments [18].

In Sweden, Mirzaei et al. report an annual capacity loss of about 1.7% for a 1 MW/1 MWh battery participating in both day ahead and FCR markets. They also demonstrate that explicitly modelling calendar and cycle ageing in the optimisation process can reduce degradation by up to 29%, while having almost no effect on profitability [11].

Despite these valuable contributions, several gaps remain. For instance most existing studies focus on optimizing operation and increasing profit, with less attention given to how these strategies affect battery degradation. As a result, the impact of different FCR services on battery lifetime is not well studied. In addition, FCR services are often analysed together or under different assumptions, which makes it difficult to directly compare their effects on both degradation and economic performance. Therefore, the link between battery ageing and profitability under realistic Nordic FCR operation remains unclear.

1.3 Purpose of the Thesis and Contributions

To address these gaps, this thesis aims to investigate battery degradation and the economic performance of BESS providing FCR in the Nordic area. This thesis specifically aims to use ageing models based on experimental data to quantify calendar and cycling ageing under different FCR services and to compare the three services to assess their impact on total battery ageing and economic performance.

This thesis are summarized as follows:

1. Development of a BESS modeling framework for Nordic FCR services (FCR-N, FCR-D up/down and combined services) in compliance with ENTSO-E requirements and applying SOC management based on energy management states (NEM/AEM).

2. Parameterization of calendar and cycling ageing models using experimental data, where calendar ageing is expressed as a function of time and SOC, and cycling ageing is modeled as a function of ΔSOC, C-rate, mean SOC, and EFCs.

3. Development of a dynamic ageing model based on the derivatives of calibrated calendar and cycling ageing models to continuously quantify degradation across all FCR services.

4. Analysis of the impact of SOC deadband selection and micro-cycles on battery degradation across different FCR services.

5. Comparison of battery degradation and economic performance for FCR services by linking ageing results with revenue.

1.4 Thesis Outline

This thesis is organized into nine chapters:

- **Chapter 1** introduces the research background, objectives, and main contributions of the thesis.

- **Chapter 2** presents the theoretical foundations of frequency control and ancillary services in power systems.

- **Chapter 3** provides the theoretical background of lithium-ion batteries.
- **Chapters 4 and 5** describe the system setup, case studies, and battery pack design.
- **Chapter 6** develops and validates the battery ageing model.
- **Chapter 7** Presents the methodology in order to evaluate battery performances.
- **Chapter 8** presents the results and discussion, including technical and economic evaluations.
- **Chapter 9 and 10** Conclude the thesis and outline directions for future research.

CHAPTER 2

Theory 1: Frequency Control and Ancillary Services in Power Systems

2.1 Power System Frequency Dynamics

2.1.1 Frequency as a Stability Indicator

The frequency of a power system reflects the real-time balance between power input from generation (P_{in}) and electrical power consumption (P_{cons}) [19]. An excess of generation relative to consumption increases frequency, while a deficit decreases it. The primary goal of frequency control is to maintain this equilibrium within an acceptable tolerance band ($\pm 0.1\,\mathrm{Hz}$) to ensure proper operation of connected apparatus and prevent equipment damage [20].

2.1.2 The Swing Equation and Inertia

In power systems, inertia, provided by the kinetic energy stored in the rotating masses of synchronous machines (generators and turbines), resists rapid frequency changes caused by power imbalances. The inertia constant H is defined as the time a machine can supply its rated power using only its stored

kinetic energy[21]. The swing equation describes this dynamic behavior,

$$\frac{2H}{\omega_s}\frac{d^2\delta}{dt^2} = P_m - P_e - D\Delta\omega, \tag{2.1}$$

where H is the inertia constant (s), ω_s is the synchronous speed (rad/s), δ is the rotor angle (rad), P_m and P_e are the mechanical and electrical powers (pu), D is the damping coefficient, and $\Delta\omega$ is the speed deviation (rad/s). Higher system inertia slows frequency deviations, allowing control mechanisms more time to respond [22].

2.1.3 Inertia in Traditional and Modern Grids

In traditional power systems, synchronous generators provide substantial inertia, stabilizing frequency. However, the rise of inverter-based renewable energy sources, such as wind and solar, which are lacking inherent inertia, increases the risk of rapid frequency fluctuations [23]. Higher inertia results in faster frequency recovery compared to systems with lower inertia. This highlights the critical role of frequency ancillary services in compensating for reduced inertia and maintaining grid stability[24, 25].

2.2 Overview of Frequency Ancillary Services

Frequency ancillary services manage frequency deviations across different time scales to maintain grid stability [20]. Frequency ancillary services include Fast Frequency Response (FFR), FCR, Automatic Frequency Restoration Reserve (aFRR), Manual Frequency Restoration Reserve (mFRR), and Replacement Reserve (RR). Each service addresses specific aspects of frequency control, from immediate stabilization to long-term balance [26, 27].

2.2.1 Comparison of Activation and Control Mechanisms

The key characteristics of frequency ancillary services include activation times, roles, and control mechanisms are summarized in Table 2.1, based on European Network of Transmission System Operators for Electricity (ENTSO-E) standards [20]. The first line of defense against frequency deviations is provided by FFR and FCR, which both activate within seconds using the automatic

droop control. These services are designed to rapidly reserve frequency deviations and stabilize the system. In contrast, aFRR and mFRR operate over longer timeframes to restore frequency to its nominal value and support system recovery [28].

Table 2.1: Comparison of frequency ancillary services based on activation times, roles, and control methods [20].

	FFR	**FCR**	**aFRR**	**mFRR**
Activation	<2 s	<15 s	30 s to 300 s	300 s to 900 s
Role	Rapid stabilize	Stabilize freq.	Restore freq.	Support restore
Control	Automatic	Automatic	Automatic	Manual

2.3 Frequency Containment Reserve (FCR)

FCR is one of the primary mechanisms for stabilizing frequency deviations, focusing on its operation, and energy management strategies for Limited Energy Reservoir (LER) assets. FCR is an automatic service that activates within seconds to limit frequency deviations caused by disturbances, such as generator outages or load changes, preventing system instability [29].

2.3.1 FCR Activation and Control

In the Nordic power system, FCR comprises FCR-N and FCR-D, which are traded in advance and activated based on frequency deviations. These services use droop control to adjust power output proportionally to frequency changes. While FCR-N is designed to continuously manage small, stochastic frequency variations around the nominal frequency, FCR-D is intended to rapidly respond to larger system disturbances. The main technical and operational characteristics governing the activation behavior of FCR-N and FCR-D are summarized in Table 2.2.

Table 2.2: Summary of Frequency Containment Reserves

Parameter	**FCR-N (Normal Operation)**	**FCR-D (Disturbance Operation)**
Purpose	Manages short-term stochastic variations in power to improve frequency quality.	Addresses larger frequency disturbances, supplementing FCR-N.
Operation	Symmetrical (production and consumption).	Non-symmetrical; Up and Down traded separately.
Frequency Range droop	49.9 Hz to 50.1 Hz	Up: 49.5 Hz to 49.9 Hz Down: 50.1 Hz to 50.5 Hz
Activation Time	63% in 60 s, 100% in 3 min.	50% in 5 s, 100% in 30 s.
Endurance	1 h	20 min
Minimum Bid Size	0.1 MW	0.1 MW

2.3.1.1 Droop Control Mechanism

FCR employs droop control to adjust power output in response to grid frequency deviations, ensuring stability in power systems. For FCR-N, the power output $P_{\text{FCR-N}}$ is modulated based on the frequency f relative to the nominal frequency $f_0 = 50\,\text{Hz}$, as defined in (2.2). The response is linear within the frequency range of 49.9 Hz to 50.1 Hz, with a maximum deviation $\Delta f^{\max}_{\text{FCR-N}} = 0.1\,\text{Hz}$, and saturates at the maximum capacity $P^{\text{Max}}_{\text{FCR-N}}$ for larger deviations [30]

$$P_{\text{FCR-N}} = P^{\text{Max}}_{\text{FCR-N}} \times \begin{cases} 1, & \text{if } f \leq 49.9\,\text{Hz}, \\ \dfrac{f_0 - f}{\Delta f^{\max}_{\text{FCR-N}}}, & \text{if } 49.9\,\text{Hz} \leq f \leq 50.1\,\text{Hz}, \\ -1, & \text{if } f \geq 50.1\,\text{Hz}, \end{cases} \tag{2.2}$$

where $f_0 = 50\,\text{Hz}$, $\Delta f^{\max}_{\text{FCR-N}} = 0.1\,\text{Hz}$, and $P^{\text{Max}}_{\text{FCR-N}}$ is the maximum FCR-N capacity [30]. For FCR-D, which addresses larger frequency deviations, the upward ($P_{\text{FCR-Dup}}$) and downward ($P_{\text{FCR-Ddown}}$) regulations are defined in (2.3) and (2.4). Upward regulation activates for frequencies between 49.5 Hz and 49.9 Hz, with a maximum deviation $\Delta f^{\text{Max}}_{\text{FCR-D}} = 0.4\,\text{Hz}$, while downward

regulation operates between 50.1 Hz and 50.5 Hz.

$$P_{\text{FCR-Dup}} = P^{\text{Max}}_{\text{FCR-Dup}} \times \begin{cases} \dfrac{f_0 - f}{\Delta f^{\text{Max}}_{\text{FCR-D}}}, & \text{if } 49.5\,\text{Hz} \leq f \leq 49.9\,\text{Hz}, \\ 1, & \text{if } f \leq 49.5\,\text{Hz}, \\ 0, & \text{otherwise}, \end{cases} \tag{2.3}$$

$$P_{\text{FCR-Ddown}} = P^{\text{Max}}_{\text{FCR-Ddown}} \times \begin{cases} \dfrac{f - f_0}{\Delta f^{\text{Max}}_{\text{FCR-D}}}, & \text{if } 50.1\,\text{Hz} \leq f \leq 50.5\,\text{Hz}, \\ 1, & \text{if } f \geq 50.5\,\text{Hz}, \\ 0, & \text{otherwise}, \end{cases} \tag{2.4}$$

Figure 2.1 illustrates the activation profiles for FCR-N, FCR-D Up and FCR-D Down as a function of frequency, showing the linear droop response and saturation points as defined in (2.2)–(2.4). These profiles demonstrate how FCR-N and FCR-D effectively stabilize frequency by adjusting power output in response to deviations.

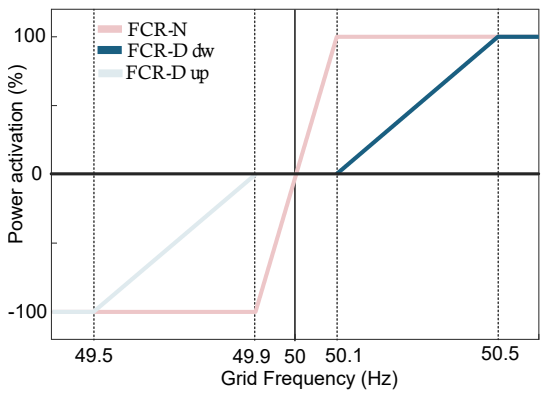

Figure 2.1: FCR activation profiles for FCR services as a function of frequency (2.2)–(2.4).

2.3.2 Providers and Technologies

Traditional providers, such as hydroelectric and thermal generators, deliver reliable FCR due to their large energy reserves [21]. Emerging providers, including BESS,that can provide Vehicle to grid (V2G), and wind turbines

with synthetic inertia, offer faster response times but are limited by energy capacity, classifying them as Limited assets, LER [31, 32].

2.3.3 Energy and Capacity Requirements

LER assets must meet specific requirements for FCR-N and FCR-D. For FCR-N, assets reserve energy for 1 h of full capacity and 34% of sold capacity for State Of Energy (SOE) restoration, requiring a rated power 1.34 times the sold capacity. For FCR-D, assets reserve energy for 20 min (0.33 MW h per MW) and 20% of energy in the opposite direction for recovery [30]. Table 2.3 presents these requirements for a 1 MW/1 MW h BESS.

2.3.4 State of energy management for battery storage

LER assets providing FCR rely on effective SOE management to maintain appropriate energy margins. Two strategies are employed: NEM and AEM, which adjust SOE based on adaptive thresholds.

2.3.4.1 Normal Energy Management (NEM)

NEM ensures adequate energy availability for FCR operation by applying a power adjustment, NEM is active when the grid frequency deviation $|\Delta f|$ is within ± 100 mHz of the nominal 50 Hz and at specific SOE thresholds, ($\mathrm{SOE}_{\text{enable, NEM}}$) and deactivates at target levels ($\mathrm{SOE}_{\text{disable, NEM}}$)

$$K_{\mathrm{NEM}}(t) = \begin{cases} +1 & \text{if } |\Delta f| < 100\,\text{mHz and SOE} > \mathrm{SOE}_{\text{enable, NEM, upper}} \\ -1 & \text{if } |\Delta f| < 100\,\text{mHz and SOE} < \mathrm{SOE}_{\text{enable, NEM, lower}} \\ 0 & \text{otherwise} \end{cases} \tag{2.5}$$

The SOE thresholds for NEM activation are defined as

$$\mathrm{SOE}_{\text{enable, NEM, upper}} = 1 - C_{\text{FCR-X}} \cdot \frac{T_{\text{endurance}}}{60} / E \tag{2.6}$$

$$\mathrm{SOE}_{\text{enable, NEM, lower}} = C_{\text{FCR-X}} \cdot \frac{T_{\text{endurance}}}{60} / E \tag{2.7}$$

where $C_{\text{FCR-X}}$ is the FCR-N or FCR-D capacity, $T_{\text{endurance}}$ is the remaining endurance (30 minutes for FCR-N and 20 minutes for FCR-D), and E is the energy capacity of the storage system.

Table 2.3: Energy and power requirement verification for FCR-N and FCR-D using a 1 MW/1 MW h BESS

Case	Requirement & Calculation	Verification & Result
	FCR-N Only (0.5 MW symmetrical)	
Operating Conditions	Reference power: 0 MW, Initial SOE: 0.5 MW h	Target capacity: 0.5 MW
Power Requirement	$1.34 \times C_{\text{FCR-N}} = 1.34 \times 0.5\,\text{MW} = 0.67\,\text{MW}$	BESS power rating: 1 MW $0.67 \leq 1\,\text{MW}$ ✓ **Satisfied**
Energy Requirement	$C_{\text{FCR-N}} = 0.5\,\text{MWh} \leq E_0$ and $\leq E_{\max} - E_0$	BESS energy: 1 MW h $0.5 \leq 0.5\,\text{MWh}$ and $0.5 \leq 0.5\,\text{MWh}$ ✓ **Satisfied**
Conclusion	System supports 0.5 MW FCR-N, constrained by energy storage capacity	
	FCR-D Up Only (1.0 MW up-regulation)	
Operating Conditions	Reference power: 0 MW, Initial SOE: 1.0 MW h	Target capacity: 1.0 MW
Power Requirement	$C_{\text{FCR-D,up}} = 1.0\,\text{MW} \leq P_p$ $0.2 \times C_{\text{FCR-D,up}} = 0.2\,\text{MW} \leq P_c$	BESS power rating: 1 MW $1.0 \leq 1\,\text{MW}$ and $0.2 \leq 1\,\text{MW}$ ✓ **Satisfied**
Energy Requirement	$\frac{1}{3} \times C_{\text{FCR-D,up}} = 0.33\,\text{MWh} \leq E_0$	BESS energy: 1 MW h $0.33 \leq 1.0\,\text{MWh}$ ✓ **Satisfied**
Conclusion	System supports 1.0 MW FCR-D up, limited by production capacity	
	FCR-D Down Only (1.0 MW down-regulation)	
Operating Conditions	Reference power: 0 MW, Initial SOE: 0 MW h	Target capacity: 1.0 MW
Power Requirement	$C_{\text{FCR-D,down}} = 1.0\,\text{MW} \leq P_c$ $0.2 \times C_{\text{FCR-D,down}} = 0.2\,\text{MW} \leq P_p$	BESS power rating: 1 MW $1.0 \leq 1\,\text{MW}$ and $0.2 \leq 1\,\text{MW}$ ✓ **Satisfied**
Energy Requirement	$\frac{1}{3} \times C_{\text{FCR-D,down}} = 0.33\,\text{MWh} \leq E_{\max} - E_0$	BESS capacity: 1 MW h $0.33 \leq 1.0\,\text{MWh}$ ✓ **Satisfied**
Conclusion	System supports 1.0 MW FCR-D down, sufficient capacity available	

A 5-minute rolling average generates the control signal

$$K_{\overline{\text{NEM}}}(t) = \frac{1}{300} \sum_{n=1}^{300} NEM_{\text{Allowed}}(t-n) \tag{2.8}$$

The total power setpoint combines FCR and NEM contributions

$$P_{\text{total}}(t) = P_{\text{FCR}}(t) + P_{\text{NEM}}(t) \tag{2.9}$$

where $P_{\text{NEM}} = 0.34 \cdot C_{\text{FCR-N}} \cdot K_{\overline{\text{NEM}}}(t)$ for FCR-N and $P_{\text{NEM}} = 0.20 \cdot C_{\text{FCR-D}} \cdot K_{\overline{\text{NEM}}}(t)$ for FCR-D. Providers can choose higher charging or discharging rates up to a maximum of 50% for FCR-N and 34% for FCR-D. Figure 2.2 shows the influence of NEM on the total power set point $P_{\text{total}}(FCR{+}NEM)$ during the activation of the FCR. The plot shows P_{total} in blue, FCR contribution in red, and NEM adjustment in gray over time. The NEM reduces the total power setpoint, moderating the rate at which power changes in order to maintain the SOE within operational limits[33].

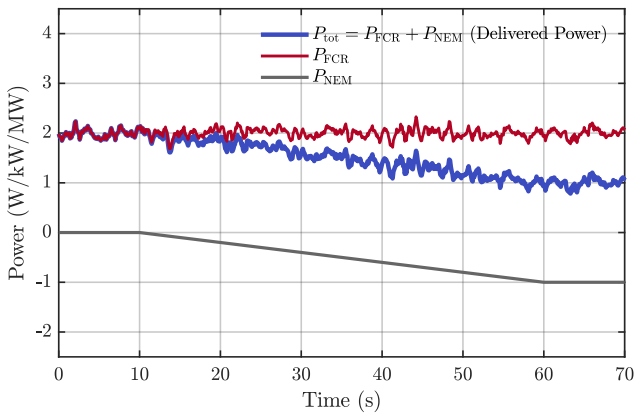

Figure 2.2: Effect of NEM on Total Power Setpoint During FCR Activation

2.3.4.2 Alert Energy Management (AEM)

AEM activates when the SOE of an FCR providing entity falls outside the operational range $[\text{SOE}_{\text{enable, AEM, lowerr}}, \text{SOE}_{\text{enable, AEM, upper}}]$. The thresholds are defined as

$$\mathrm{SOE}_{\text{enable, AEM, upper}} = 1 - C_{\text{FCR-X}} \times \frac{T_{\text{endurance}}}{60}/E \tag{2.10}$$

$$\mathrm{SOE}_{\text{enable, AEM, lower}} = C_{\text{FCR-x}} \times \frac{T_{\text{endurance}}}{60}/E \tag{2.11}$$

where $C_{\text{FCR-X}}$ is the FCR-N or FCR-D capacity and E is the energy capacity of the storage system. These thresholds allow a smooth deactivation of the steady-state FCR response over 5 to 10 minutes. The frequency reference during AEM is set to the nominal value $f_0 = 50\,\text{Hz}$ outside the critical SOE range, as defined by

$$f_{\text{AEM}}(t) = \begin{cases} f_0 & \text{if SOE} \notin [\mathrm{SOE}_{\text{enable, AEM, lower}}, \mathrm{SOE}_{\text{enable, AEM, upper}}] \\ f(t) & \text{otherwise} \end{cases} \tag{2.12}$$

A smoothed frequency reference is calculated using a 5-minute rolling mean with 1 second resolution[33]

$$f_{\text{ref}}(t_i) = \frac{1}{300} \sum_{n=1}^{300} f_{\text{AEM}} \tag{2.13}$$

CHAPTER 3

Theory 2: Lithium-ion-battery

3.1 The Electrochemical Cell

The electrochemical cell is the fundamental unit of a battery and is responsible for the conversion between chemical and electrical energy. During the discharge, chemical energy is converted into electrical energy, while the charging phase involves the conversion of electrical energy back into chemical energy.

A typical electrochemical cell consists of two electrodes, a positive and a negative electrode separated by a separator. The electrodes serve as the locations where oxidation (anode) and reduction (cathode) reactions occur. During discharge, electrons flow from the negative electrode working as anode to the positive electrode working as cathode) through the external circuit, while ions migrate through the electrolyte to maintain charge neutrality.

During discharge:

$$\mathrm{LiC_6} \longrightarrow \mathrm{C_6} + \mathrm{Li^+} + \mathrm{e^-}$$

$$\mathrm{Li_{1-x}MO_2} + \mathrm{xLi^+} + \mathrm{xe^-} \longrightarrow \mathrm{LiMO_2}$$

During charge: the reverse process occurs, resulting in the full-cell reaction

$$\mathrm{Li}_{1-x}\mathrm{MO}_2 + \mathrm{Li}_x\mathrm{C}_6 \underset{\text{discharge}}{\overset{\text{charge}}{\rightleftharpoons}} \mathrm{LiMO}_2 + \mathrm{C}_6, \quad 0 < x < 1 \tag{3.1}$$

where MO represent a metal oxide. Electrodes contain active materials which can be pure metallic or belonging to an insertion type. Metallic electrodes facilitate reactions only at their surface, whereas insertion electrodes allow redox reactions to occur throughout their bulk structure, providing higher capacity and improved reversibility[34].

The electrolyte acts as an ionic medium enabling the movement of ions between the two electrodes. It usually contains one or more salts dissolved in solvent. The electrolyte should have high ionic conductivity, strong chemical and electrochemical stability, and good compatibility with both electrodes. Liquid electrolytes composed of Lithium hexafluorophosphate ($LiPF_6$) dissolved in organic carbonates such as ethylene carbonate (EC), dimethyl carbonate (DMC) or diethyl carbonate (DEC) offer high ionic mobility but limited mechanical strength[34].

A separator is a porous polymeric membrane that is saturated with an electrolyte solution. The role of the separator is to prevent direct interaction between the electrodes in order to avoid internal short circuits. The separator must exhibit high porosity, robust mechanical integrity, thermal stability, and excellent wettability with the electrolyte[34].

The current collectors function as conductors enabling the transfer of electrons between electrodes and the external circuit. These collectors are composed of thin metal foils: aluminum for the positive electrode and copper for the negative electrode, chosen due to their excellent electrical conductivity and chemical stability.

The casing provides mechanical protection, containment, and environmental stability. It prevents evaporation or degradation of the electrolyte and to various extent protects internal components from mechanical damage or contamination. The performances of an electrochemical cell depend on material selection and cell design[34],[35]. Figure 3.1 shows an electrochemical cell, illustrating the migration of lithium ions between the two electrodes.

3.2 Lithium-Ion Cell Properties

The operation of a lithium-ion cell is driven by fundamental electrochemical processes. During charge and discharge, lithium ions move between the

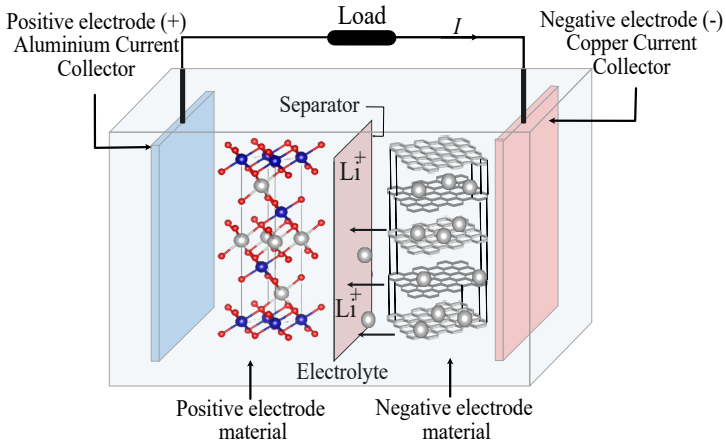

Figure 3.1: Schematic of a lithium-ion battery illustrating lithium-ion transport between the negative and positive electrode during operation.

negative and positive electrodes through the electrolyte, while electrons flow through the external circuit to provide power. These movements of ions and electrons determine key characteristics of the battery such as voltage, capacity, and internal resistance.

These characteristics are described using electrical variables that relate the internal electrochemical processes to measurable quantities.

The SOC represents the remaining charge in the battery relative to its nominal capacity and is defined as

$$\mathrm{SOC}(t) = \frac{Q_{\mathrm{remaining}}(t)}{Q} \tag{3.2}$$

where $Q_{\mathrm{remaining}}(t)$ is the available charge in the cell at time t, and Q is the nominal capacity of the battery.

The open circuit voltage (OCV) corresponds to the equilibrium voltage of the cell when no current is flowing. It is a nonlinear function of SOC and reflects the difference in electrochemical potentials between the electrodes.

The capacity of a lithium-ion cell, expressed in ampere hours (Ah), represents the total charge that can be delivered. This capacity decreases over time due to ageing of the cells.

The energy flowing in and out of the battery is given by

$$E(t) = \int V_{\text{batt}}(t)\, i_{\text{cell}}(t)\, dt \tag{3.3}$$

while the instantaneous power flowing in and out of the batteryis defined as

$$P(t) = V_{\text{batt}}(t)\, i_{\text{cell}}(t) \tag{3.4}$$

where $P(t)$ is the instantaneous power, $V_{\text{batt}}(t)$ is the terminal voltage of the battery, and $i_{\text{cell}}(t)$ is the cell current. The power capability is limited by internal resistance and thermal constraints, which lead to increased losses at high current levels.

Finally, the C-rate describes the charge or discharge current relative to the nominal capacity, where a rate of 1C corresponds to a full charge or discharge in one hour.

Lithium-ion batteries typically should be operated temperature range of 10–35°C [36]. The temperature variations significantly influence cell performance. Elevated temperatures accelerate parasitic side reactions, such as growth of the Solid Electrolyte Interphase (SEI), which accelerate capacity degradation. In contrast, at lower temperatures, the ionic conductivity of the electrolyte decreases and the resistance to charge transfer increases [37].

Lithium-ion batteries gradually lose capacity over time, both duing storage and during operation. Ageing is typically classified into calendar ageing, which occurs during periods of rest and is effected by storage conditions such as temperature and SOC, and cycling ageing, which results from battery operation [38], [39]. Calendar ageing mainly occurs because of ongoing chemical side reactions, such as the continuous growth of the SEI layer on the negative electrode, electrolyte decomposition, and transition metal dissolution from the positive electrode.

Cycling ageing instead arises from mechanical and electrochemical stresses caused by lithiation and delithiation, including electrode expansion and contraction, lithium plating on the negative electode, and cracking of active material particles. The magnitude of these strongly depends on operating parameters such as the C-rate, the SOC window and number of cycles [39]. Table 3.1, summarises the key differences between calendar and cycling ageing in LFP batteries.

Table 3.1: Ageing Modes and Mechanisms in LFP Batteries

	Calendar	Cycling
Mechanisms	SEI growth	SEI growth, plating, cracking
Key factors	High T, high SOC	large SOC window, high C-rate, T>25°C

3.3 Lithium-Ion Cell Modelling

To capture and predict the behaviour described in the previous sections, mathematical models are employed to represent the electrochemical cell. Battery modelling bridges the gap between physical processes and system-level performance, supporting evaluation, control, and optimization.

3.3.1 Equivalent Circuit Model (ECM)

The equivalent Circuit Model (ECM) provides an empirical representation of electrochemical processes in lithium-ion batteries by using electrical elements such as resistors, capacitors, and voltage sources. This approach allows fast simulation of voltage, current and SOC. A first-order RC ECM is presented in figure 3.2[40].

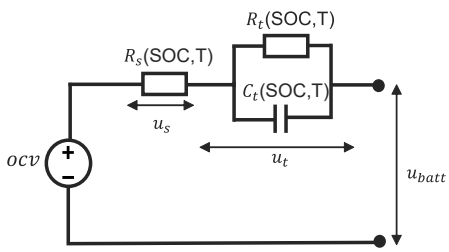

Figure 3.2: Schematic of the first-order RC equivalent circuit model for a lithium-ion battery.

The terminal voltage is determined by

$$V_{\text{batt}}(t) = \text{ocv}(t) - u_t(t) - i_{\text{cell}}(t)R_s, \tag{3.5}$$

where *ocv(t)* is the open circuit voltage. $u_t(t)$ is the voltage drop across the

parallel RC branch which in principe models the diffusion-limited and charge-transfer polarization effects. Resistance R_1 mainly models the charge-transfer resistance while capacitance C_1 mainly represents the double-layer capacitance at the electrode-electrolyte interfaces. $i_{\text{cell}}(t)$ is the current and R_s is the series resistance, presenting ohmic losses due to electrical resistance of the electrode materials, current collectors, and ionic resistance of the electrolyte. The dynamics of the RC branch and SOC are determined by

$$\frac{du_t(t)}{dt} = -\frac{u_t(t)}{R_1 C_1} + \frac{i_{\text{cell}}(t)}{C_1}, \quad \frac{d\text{SOC}(t)}{dt} = -\frac{i_{\text{cell}}(t)}{Q}, \tag{3.6}$$

3.3.2 Ageing models for calendar and cycling degradation

To quantify and predict ageing, semi-empirical models are commonly used to quantify battery ageing. These models describe how capacity loss changes as a function of temperature, SOC, charge throughput and C-rate. These models provide mathematical expressions that capture the dominant stress factors associated with calendar and cycling ageing [38]. A commonly adopted semi-empirical model to describe calendar ageing losses is expressed by

$$\Delta Q_{\text{loss, cal}} = A\, e^{-E_a/(RT)}\, \text{SOC}^{\alpha}\, t^{z} \tag{3.7}$$

where A is a pre-exponential factor, E_a is the activation energy, R is the universal gas constant, T is the temperature, α and z are fitted parameters derived from experiments and t is the storage time [41], [42].

Concerning the capacity loss associated with cycling, the loss can be described by

$$Q_{\text{loss}} = \delta \cdot \exp\left(-\frac{E_a}{RT}\right) (Ah)^{z} \tag{3.8}$$

where δ is the pre-exponential factor, E_a is the activation energy, R is the gas constant with value $8.314\,\text{J}/(\text{K}\cdot\text{mol})$, T is the absolute temperature, z is the power-law factor and Ah is the ampere hour throughput [38], [43].

3.4 Composing cells into battery packs

The BESS consists of multiple cells. These cells are first grouped into modules and then several modules are connected in series to create a battery string that

provides the required operating voltage. To increase the total energy and current that the system requires, multiple strings are connected in parallel, forming the complete battery pack.

The number of parallel strings required to meet the total energy specification of the battery is calculated as

$$m_{\text{strings}} = \frac{E_{\text{batt}}}{U_{\text{batt}}^{\text{nom}} Q_{\text{cell}}}, \qquad m_{\text{strings}} \in \mathbb{N}, \tag{3.9}$$

where E_{batt} is the desired energy capacity, $U_{\text{batt}}^{\text{nom}}$ the nominal pack voltage, and Q_{cell} the nominal capacity of a single cell.

The current flowing through a single cell is given by

$$i_{\text{cell}}(t) = \frac{p_{\text{batt}}(t)}{u_{\text{batt}}(t)} \frac{1}{m_{\text{strings}}} \tag{3.10}$$

To achieve the required pack voltage, cells are connected in series. The number of series-connected cells is given by

$$n_{\text{cell}} = \left\lceil \frac{U_{\text{batt}}^{\text{nom}}}{U_{\text{cell}}^{\text{nom}}} \right\rceil \tag{3.11}$$

where $U_{\text{cell}}^{\text{nom}}$ denotes the nominal voltage of an individual cell. The total energy content of the resulting battery pack becomes

$$E_{\text{batt}} = U_{\text{cell}}^{\text{nom}}\, n_{\text{cell}}\, Q_{\text{cell}}\, m_{\text{strings}}. \tag{3.12}$$

3.5 Economic Modelling

The economic value of BESS can be assessed using its NPV [44]. The NPV of a battery can be expressed by

$$C^{\text{bat}} = (1 - r^{\text{SV}}) \frac{C^{\text{REP}}}{(1+i)^L} + C^{\text{OM}} \frac{(1+i)^L - 1}{i(1+i)^L}\, C^{\text{REP}} \tag{3.13}$$

where C^{REP} is the battery replacement cost, i is the interest rate, C^{OM} represents the operation and maintenance cost of the battery cost per year, L is the estimated lifetime of the battery, EOL is the end-of-life of battery and r^{SV} is the salvage value ratio, which represente the revenue that can be recovered

from recycling or selling battery parts at the end of life. The cost associated with calendar ageing or cycling ageing is calculated based on

$$\text{Cost}^{\text{cal/cyc}} = C^{\text{bat}} \frac{\Delta Q_{\text{loss, cal/cyc}}}{100\% - \text{EOL (\%)}} \tag{3.14}$$

where $Q_{\text{loss, cal/cyc}}$ is the capacity loss due to calendar/cycling ageing. The annual profit is calculated by subtracting the degradation costs from the market revenue. This can be mathematically represented as

$$\text{Profit}_{\text{annual}} = \text{Revenue}_{\text{market}} - \left(\text{Cost}^{\text{cal}} + \text{Cost}^{\text{cyc}}\right) \tag{3.15}$$

where $\text{Revenue}_{\text{market}}$ represents the income from market participation, while Cost^{cal} and Cost^{cyc} account for calendar and cycling degradation [45].

3.6 Rain-flow counting

Rainflow counting is a cycle counting method used in fatigue analysis to convert irregular load or stress time series into equivalent fatigue cycles. The method was introduced by Matsuishi and Endo in 1968 [46]. It operates by identifying local extrema in the signal and evaluating successive sets of four points to extract individual cycles; S_i, S_{i+1}, S_{i+2}, and S_{i+3}. It computes the ranges $\Delta S_1 = |S_{i+1} - S_i|$, $\Delta S_2 = |S_{i+2} - S_{i+1}|$, and $\Delta S_3 = |S_{i+3} - S_{i+2}|$. If $\Delta S_2 \leq \Delta S_1$ and $\Delta S_2 \leq \Delta S_3$, a full cycle with range ΔS_2 (between S_{i+1} and S_{i+2}) is identified, counted, and stored. The intermediate points S_{i+1} and S_{i+2} are then removed from the sequence, allowing the algorithm to extract smaller cycles first [47]. This four-point rule is applied repeatedly until no additional cycles can be identified. Any remaining unmatched extrema are treated as residual half-cycles and are either paired separately or counted as open reversals [48]. Figure 3.3 illustrates this iterative cycle detection and residue handling process. Figure 3.4 example loading sequences and the progressive extraction of cycles.

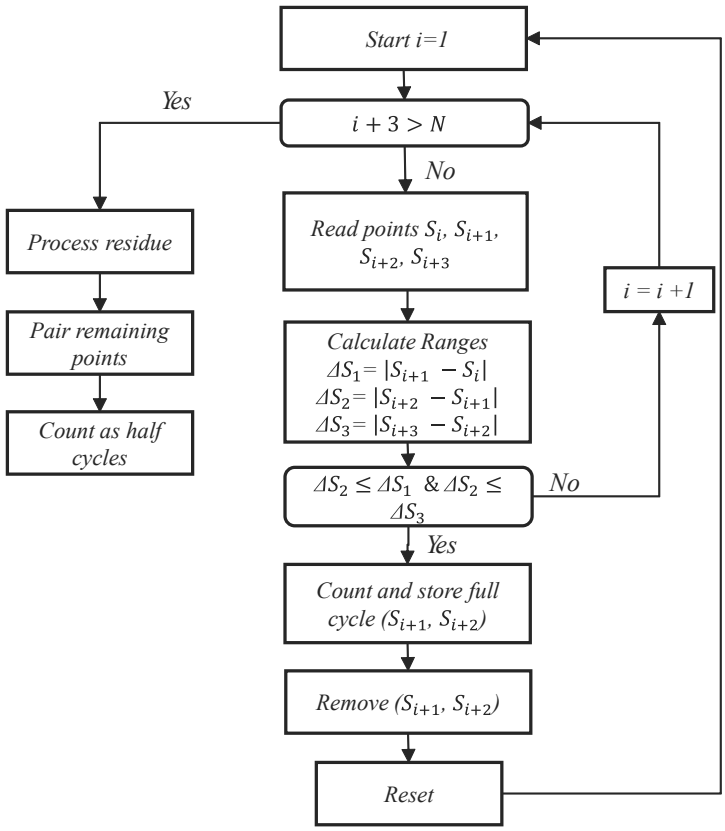

Figure 3.3: Rainflow counting algorithm: Flowchart of cycle detection and residue handling

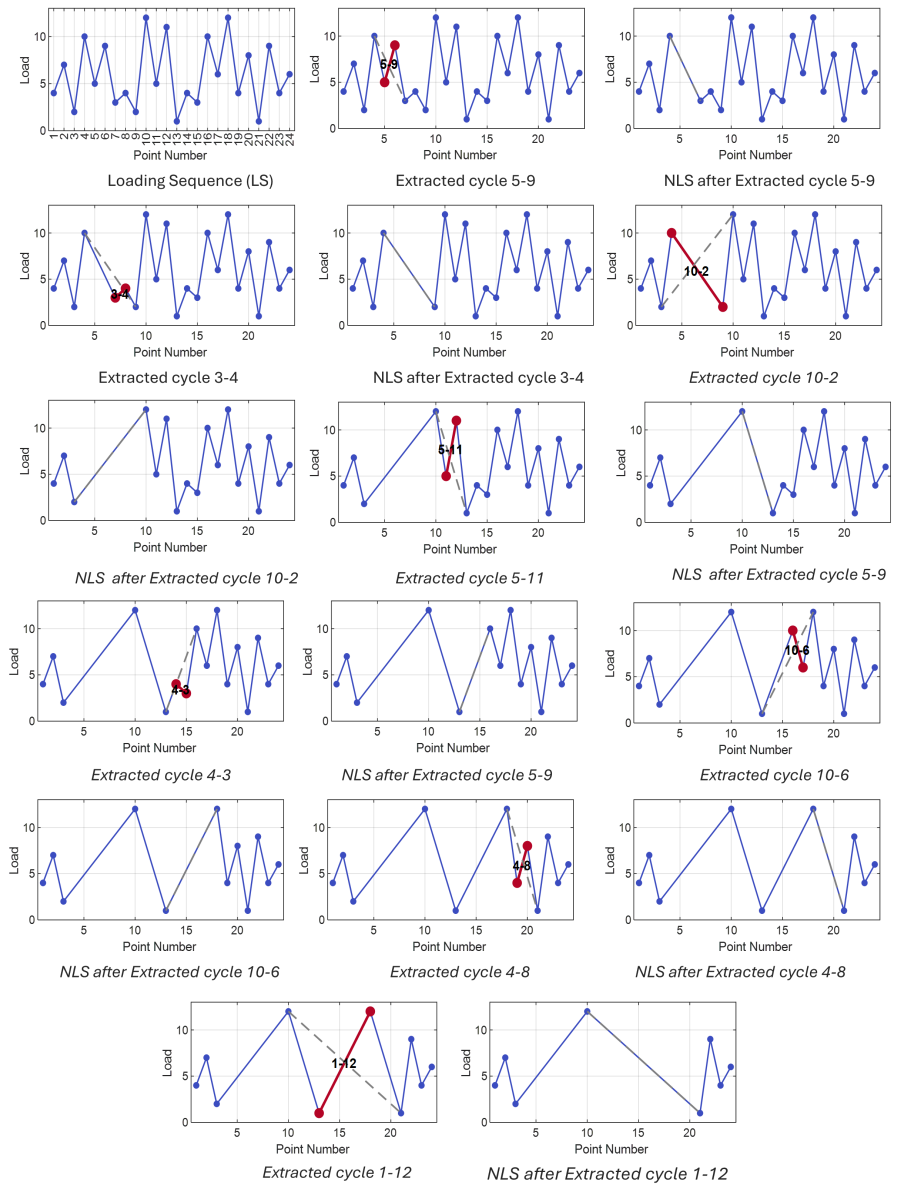

NLS: New Loading Sequence

Figure 3.4: Graphical demonstration of the Rain flow Algorithm for cycle extrac-

 tion from a Loading Sequence.

CHAPTER 4

Case set-up 1

4.1 System Description

This section describes the setup of case studies in which batteries provide FCR services, highlighting the operational conditions and inputs used for the analysis. The focus is on three specific services: FCR-N, FCR-D up, and FCR-D down. Measurement data was used to estimate degradation and the associated economic cost.

4.1.1 Battery Setup

For this case study, three identical 1 MW/1 MWh battery are deployed:

- **Battery 1:** provides FCR-N (Symmetrical service, absorbs and injects power from/to grid).
- **Battery 2:** provides FCR-D up (injects power to the grid).
- **Battery 3:** provides FCR-D down (absorbs power from the grid).

Figure 4.1 illustrates the required power ability and energy content for a 1 MW/1 MWh battery providing different FCR services as summarized table 2.3: For FCR-N, a symmetrical service, the battery delivers 0.5 MW of power

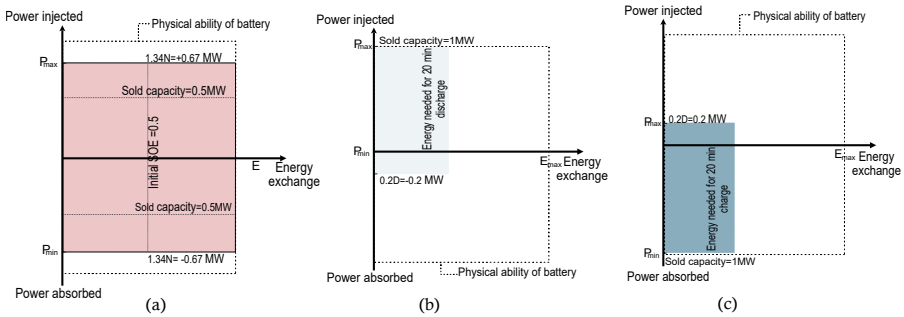

Figure 4.1: Required battery capacity and energy for each FCR service: (a) FCR-N, (b) FCR-D up, and (c) FCR-D down, based on the technical specifications outlined in Section 2.3.3. The contracted capacity is (N) 0.5 MW for FCR-N and (D) 1 MW for FCR-D services.

with an energy requirement of 1 MWh, with 0.5 MWh allocated in each direction. To allow fast adjustment of the power setpoint when the NEM is activated, 34% of the battery capacity must be reserved in each direction. For FCR-D services, the power requirements are asymmetric: for FCR-D up, the system must deliver 1 MW, while for FCR-D down, it can absorb −1 MW. Each direction has an energy requirement of 0.33 MWh, corresponding to a 20-minute endurance. Additionally, 20% of the battery capacity must be reserved in the opposite direction of each service to enable rapid setpoint changes and ensure reliable provision of the reserve. These requirements demonstrate how both nominal power and usable energy must be carefully allocated to meet technical specifications and operational flexibility for each FCR service.

4.2 Power and SOE Calculation

The power profile of each battery is determined based on the grid frequency profile and the specific FCR service requirements. Frequency data from 2022 for the Nordic region is used as the input, and the corresponding power is calculated according to each service requirement as described in Section 2.3.1.1.

To monitor the energy content within the battery, the SOE is computed by integrating the power profile over time relative to the battery's rated energy capacity E_{rated}. The SOE represents the fraction of usable energy stored

in the battery, expressed as a percentage of the total energy capacity. It is constrained between 10 % and 90 % to prolong the battery's lifetime.

In this study, SOE is used to directly capture the battery's energy during the provision of FCR services. SOE is calculated based on

$$\mathrm{SOE}(t) = \mathrm{SOE}(t_0) + \frac{1}{E_{\mathrm{rated}}} \int_{t_0}^{t} \eta \, P(t) \, dt \tag{4.1}$$

where $SOE(t_0)$ is the initial state of energy, E_{rated} is the nominal energy capacity of the battery, η represents the battery efficiency, and $P(t)$ is the battery power at time t. Positive power values correspond to discharging, while negative values indicate charging. SOE recovery is implemented based on the strategy described in Section 2.3.4. As described in Section 2.3.4, the recovery states are activated and deactivated based on predefined hysteresis thresholds.

Figure 4.2 illustrates when each SOE recovery state is activated and deactivated for the three FCR services, showing how batteries recover their SOE and preventing overcharging or excessive discharge.

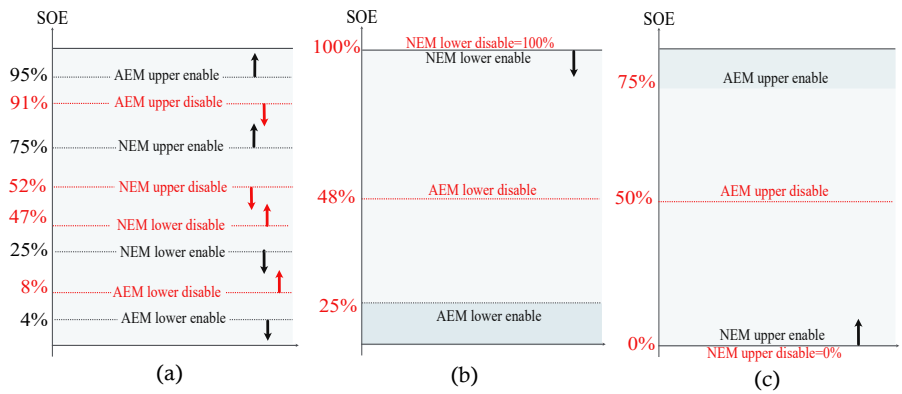

Figure 4.2: SOE recovery activation and deactivation for each FCR service **(a) FCR-N**, **(b) FCR-D up**, and **(c) FCR-D down**, based on the strategy outlined in Section 2.3.4.

4.3 Base verification

The simulation was conducted under a synthetic frequency profile designed to activate the three FCR services. These profiles were designed in order to provide the desired service with activation of the NEM state to see how it controls the battery behavior and state.

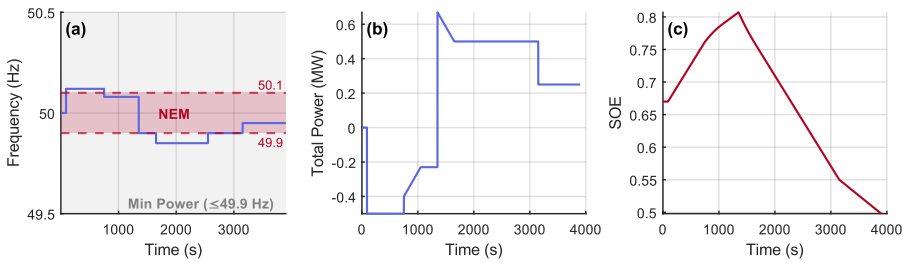

Figure 4.3: System Response: (a) Synthetic Frequency to activate FCR-N, (b) Power, and (c) SOE.

Figure 8.2 illustrates the operation of a battery providing FCR-N service, showing (a) the synthetic grid frequency, (b) the total power output, and (c) the SOE over time. Initially, the frequency exceeds 50.1 Hz, causing the battery to charge at its maximum power of -0.5 MW and increasing the SOE from 0.67 to 0.76. At $t = 751$ s, the SOE has crossed the NEM upper activation threshold of 0.75, triggering NEM. As the SOE is elevated, NEM responds in the discharge direction, gradually superimposing a positive bias of $0.34 \times C_{\text{FCR-N}} = +0.17$ MW via a 300 s rolling average. This causes the net power to shift from -0.39 MW toward -0.23 MW, effectively countering the FCR-N charging component and stopping the SOE rise. At $t = 1350$ s, the frequency drops to 49.9 Hz, committing the FCR-N response to full discharge at $+0.5$ MW. The residual NEM bias in the rolling average causes a temporary increase in total power to $+0.67$ MW. The 34% power reserved for NEM allows recovery to be applied without affecting the contracted FCR-N capacity, enabling the battery to support frequency regulation while restoring its SOE.

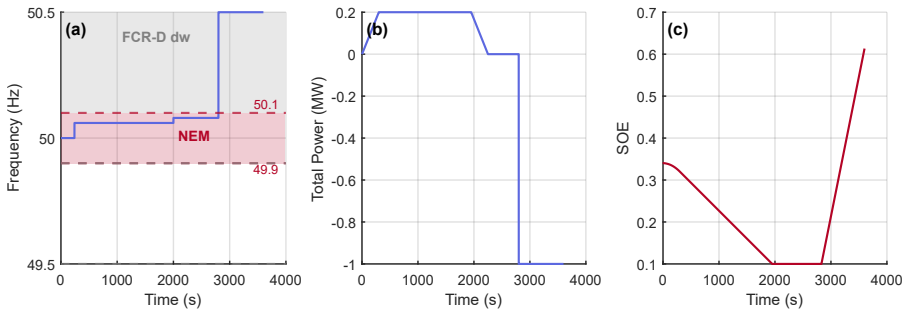

Figure 4.4: System Response: (a) Synthetic Frequency to activate FCR-D down, (b) Power, and (c) SOE.

Figure 4.4 present FCR-D down event. Initially, the frequency remains stable at 50 Hz. It then increases to 50.06 Hz, then to 50.08 Hz, remaining within the NEM range. Finally, the frequency jumps to 50.5 Hz, leaving the NEM range. During the NEM phase, the battery discharges until it reaches the critical SOE limit of 0.1. Since the battery's operating range is between 0.1 and 0.9, it stops injecting power once it reaches 0.1, even if the frequency remains within the NEM range. When the frequency rises above 50.1 Hz, the battery resumes charging to provide FCR-D down support.

Figure 4.5 illustrates the behaviour of the battery during an FCR-D up event. Initially, the frequency remains stable at 50 Hz. It then gradually decreases to 49.98 Hz, remains at that level for a short period, and is still within the NEM range. Finally, the frequency drops to 49.5 Hz, leaving the NEM range. During the NEM phase 20% of the battery operates in the opposite direction, effectively recovering energy while still providing FCR-D up support. This allows the battery to restore its SOE when it was previously discharging for FCR-D up. The battery continues charging until it reaches the critical SOE limit of 0.9. Since the battery's operating range is between 0.1 and 0.9, it stops absorbing power once it reaches 0.9, even if the frequency remains within the NEM range. When the frequency falls below 49.9 Hz, the battery resumes discharging to provide FCR-D up support.

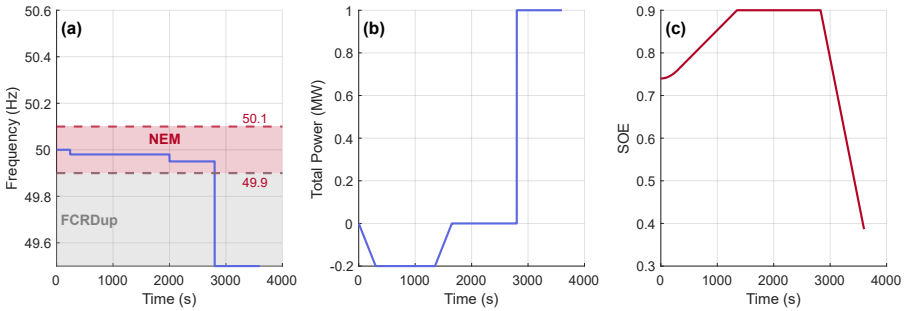

Figure 4.5: System Response: (a) Synthetic Frequency to activate FCR-D up, (b) Power, and (c) SOE.

The base verification demonstrates that the battery can track the synthetic frequency signals across all FCR services while effectively using the NEM mechanism to manage its SOE. During FCR-N events, the battery adjusts its power output dynamically to support grid frequency while allowing partial recovery of SOE. For FCR-D up and FCR-D down events, the battery operates within its prescribed limits, with the NEM mechanism acting in the opposite direction of the service to restore SOE. The findings confirm that the control strategy operates as designed, providing accurate frequency response and effective energy management.

CHAPTER 5

Case set up 2

5.1 Cell selection and specifications

For this study, a battery made up of a base the cell, tested by [49] is used. Its specifications are listed in Table 5.1.

Table 5.1: Specifications of the Sony/Murata US26650FTC1 $LiFePO_4$ cell

Parameter	**Value**
Nominal capacity	3.0 Ah
Nominal voltage	3.2 V
Max. charge voltage	3.65V
Min. discharge voltage	2.00 V
Max. continuous charge current	2.85 A
Max. continuous discharge current	20 A

5.2 Module and pack design

LFP chemistry is well suited for FCR services. These services value long cycle life and strong thermal stability more than high energy density. As FCR services are stationary grid services, weight and volume are not a constraint. In addition, LFP batteries typically exhibit lower cost compared to other lithium-ion battery chemistries.

5.2.1 Module Design: 25S9P configuration

A module is using a 25S9P arrangement of LFP cells is used in this thesis. The series connection increase the operating voltage, while the parallel branches increase the current capability and reduce effective internal resistance. Under nominal operating conditions, this configuration produces a module voltage of 80 V, a usable capacity of 27 Ah, and an energy content of 2.16 kWh. Each module contains 225 cells and serves as the fundamental building block for constructing higher voltage strings and full battery packs.

5.2.2 Series string sizing

To achieve a target DC voltage of approximately 400 V, five modules are connected in series, forming one string. This results in a string voltage of 400 V. The actual operating voltage is defined by the cell-level limits: a fully charged string reaches 456.25 V, while a fully discharged string drops to 250 V. This voltage window determines the required ratings of the power converter, insulation coordination, and pack-level protection devices.

5.2.3 Parallel string sizing for a 1 MWh pack

To achieve a total energy of 1 MWh, the required number of parallel strings is determined from the energy provided by a single series string. Each 400 V string consists of five 25S9P modules with a nominal energy of 10.8 kWh.
In order to reach 1 MWh, 93 parallel strings is required, corresponding to a total pack energy of 1004.4 kWh.

The series structure of each string remains fixed throughout the design. By keeping the series topology constant and adjusting only the number of parallel strings, the architecture remains electrically consistent while allowing diect scaling of total energy capacity.

5.3 Assumptions Regarding BMS and Power Conversion

The battery management system (BMS) and the power-conversion equipment (inverter/PCS) are essential elements for connecting the battery to the grid. However, in this study, their dynamic behaviour and efficiency characteristics are not modelled. Both are treated as ideal, assuming perfect balancing, protection, control, and loss-free power transfer. This simplification allows the analysis to focus solely on the stored energy in the battery.

CHAPTER 6

Development of the ageing model

6.1 Ageing Data and testing

The ageing models developed are based on experimental data from two long-term studies using commercial Sony/Murata US26650FTC1 LFP cells [50], [51]. The calendar ageing data originate from a 29 month storage study in which cells were kept at a fixed temperature and fixed SOC conditions, with periodic check-up measurements. The dataset includes two temperature levels and two SOC levels. The four storage conditions considered in this work are:

- 25°C, 50% SOC,
- 25°C, 100% SOC,
- 40°C, 50% SOC,
- 40°C, 100% SOC.

During the storage period, temperature was controlled using temperature chambers, and SOC was maintained via voltage holds to ensure stable open-circuit conditions. At each scheduled time, the cells were removed from storage

and characterised at 25°C using two consecutive 1C CCCV charge discharge cycles, as reported in [50]. Figure 6.1 shows how storage temperature and SOC influence calendar ageing, as anticipated. Capacity loss increases when either the temperature or the SOC is higher, with the greatest loss occurring at 40°C and 100% SOC. In comparison, cells stored at 25°C and 50% SOC show only minor ageing, which indicate that keeping both temperature and SOC low during storage is an effective way to limit irreversible capacity loss and extend battery life.

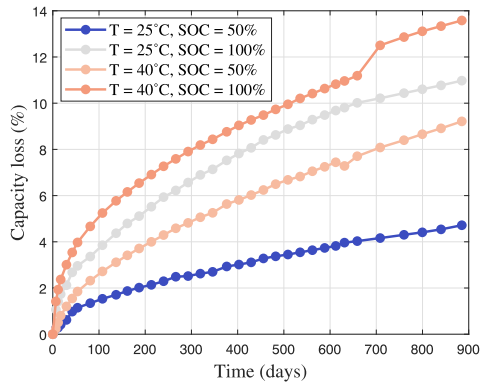

Figure 6.1: Capacity loss under different storage conditions.

The cycling ageing dataset was obtained from a complementary 29 month experiment in which a test matrix comprising of the same type of cell was subjected to continuous charge discharge cycling under controlled conditions [51]. The experiment involved altering four primary factors to determine how they contributed to degradation:

- Temperature: 25°C and 40°C,
- SOC window: 10%, 80%, and 100%,
- Mean SOC: 25%, 50%, and 75%,
- C-rate: 0.2C, 0.5C and 1C.

Figure 6.2 shows the effect of different cycling conditions on capacity loss as a function of EFC.

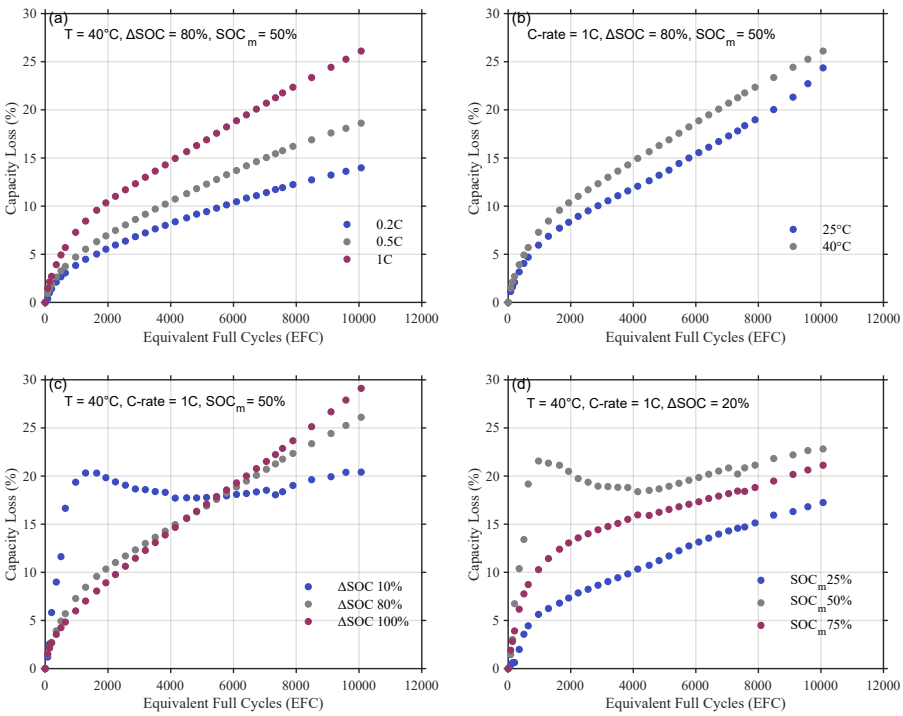

Figure 6.2: Capacity loss under different cycling conditions.2.3.4.

Fig.(a), sow that an increase of C-rate from 0.2C to 1C leads to faster degradation, with a capacity loss of 26% for 1C, compared to 14% for 0.2C. The same behaviour is observed in Fig. (b), where higher temperature (40°C) accelerate capacity loss more than at 25°C.

The strongest effect is observed in Fig. (c), where increasing ΔSOC from 10% to 100% leads to an increase in degradation. Full cycling (100%) results in 30% capacity loss, while shallow cycling (10%) remains at 20% of capacity after 10000 EFC.

Finally, Fig. (d) shows the effect of mean SOC. Operating at 75% results in higher capacity loss compared to lower SOC (25%), which indicate that degradation increases with average SOC.

6.2 Ageing model

6.2.1 Calendar Ageing model

Calendar ageing is modelled using a semi-empirical model that follows an Arrhenius-type relationship combined with power-law time dependence. This model was selected because it has been repeatedly validated for LFP chemistry in long-term storage studies. It captures exponential sensitivity of degradation to temperature, the increase in ageing at high SOC, and the sub-linear progression of capacity fade over time. The capacity loss, denoted as Q_{cal} is given by the equation

$$Q_{\text{cal}} = A\, e^{-E_a/(RT)}\, \text{SOC}^{\alpha}\, t^{n} \tag{6.1}$$

where Q_{cal} represents the capacity in percent loss, A is the pre-exponential factor, E_a is the activation energy in joules per mole, R is the universal gas constant (8.314 J/mol · K), T is the temperature in kelvin, t is the storage time in hours, α is the exponent describing the SOC dependence, and n is the time exponent. The model parameters were estimated using non-linear least-squares optimization. The objective function minimized the sum of squared residuals between measured and predicted capacity values

$$\min_{A,E_a,\alpha,n} \sum_{i=1}^{N} \left(Q_{\text{meas},i} - Q_{\text{cal}}(t_i, T_i, \text{SOC}_i)\right)^2 . \tag{6.2}$$

The fitting procedure used physical constraints: $A > 0$, $E_a > 0$, $\alpha \geq 0$, and $n > 0$.

6.2.2 Cyclic Ageing model

Cycling ageing is modelled using a semi-empirical expression that involves the influence of cycle range ΔSOC, $\mathrm{SOC_m}$, C-rate, temperature and number of cycles.

$$Q_{\mathrm{cyc}} = A \cdot (\Delta SOC)^a \cdot (SOC_{\mathrm{m}})^m \cdot (C_{\mathrm{rate}})^b \cdot e^{-E_a/(RT)} \cdot (EFC)^z \qquad (6.3)$$

where Q_{cyc} is the capacity loss (%), A is the pre-exponential scaling factor, ΔSOC is the SOC range (%) for each cycle, SOC_{m} is the mean SOC for each cycle (%), C_{rate} is the charge discharge rate, E_a is the activation energy (J/mol), R is the universal gas constant (8.314 J/mol·K), T is the temperature (K), EFC is the equivalent full cycles, and a, m, b, z are the respective exponents. The estimation of the parameter was performed using constrained nonlinear regression similar to the calendar ageing case.

6.3 Parametrization of Calendar and Cycling Ageing Models

The evaluation of the calendar and cycling ageing models focuses on how accurately they reproduce the degradation behaviour observed in long-term storage and cycling experiments. The analysis considers the influence of temperature, SOC swing, C-rate, and average SOC, and assesses the parameter values obtained from fitting each model to the experimental datasets.

6.3.1 Calendar Ageing: Model Validation and Parameter Analysis

The calendar ageing model defined in 6.1 was fitted to the experimental data shown in figure 6.1. Across all four storage conditions, the model matches the measured capacity loss. The model successfully captures the non-linear behaviour of degradation and the combined accelerating effects of elevated temperature and high SOC.

The results confirm the expected behaviour: capacity fade increases significantly with temperature and SOC. Storage at 40°C leads to faster degradation than at 25°C, and cells maintained at 100% SOC degrade more rapidly than

those stored at 50% SOC. The most pronounced ageing occurs under the combined condition of 40°C and 100% SOC.

Parameter estimation gives a pre-exponential factor of $A = 0.46$ and an activation energy of $E_a = 14.22\ \mathrm{kJ\,mol^{-1}}$, indicating moderate temperature sensitivity consistent with LFP storage behaviour. The SOC dependence is reflected in the exponent $\alpha = 0.863$, showing a strong influence of SOC on degradation rate. The A is based on SOC expressed in percentage. When SOC is expressed as a fraction, the pre-exponential factor must be adjusted accordingly, such that $A_{\mathrm{frac}} = A_{\%} \cdot 100^{\alpha}$.

The fitted time exponent $n = 0.493$ indicates that capacity loss increases at a slowing rate over time.

The model accuracy is supported by the low RMSE values, which range from 0.8584 to 0.4973 for the four conditions. The best fit occurs in 40°C and 100% SOC, where the calender degradation is the most pronounced.

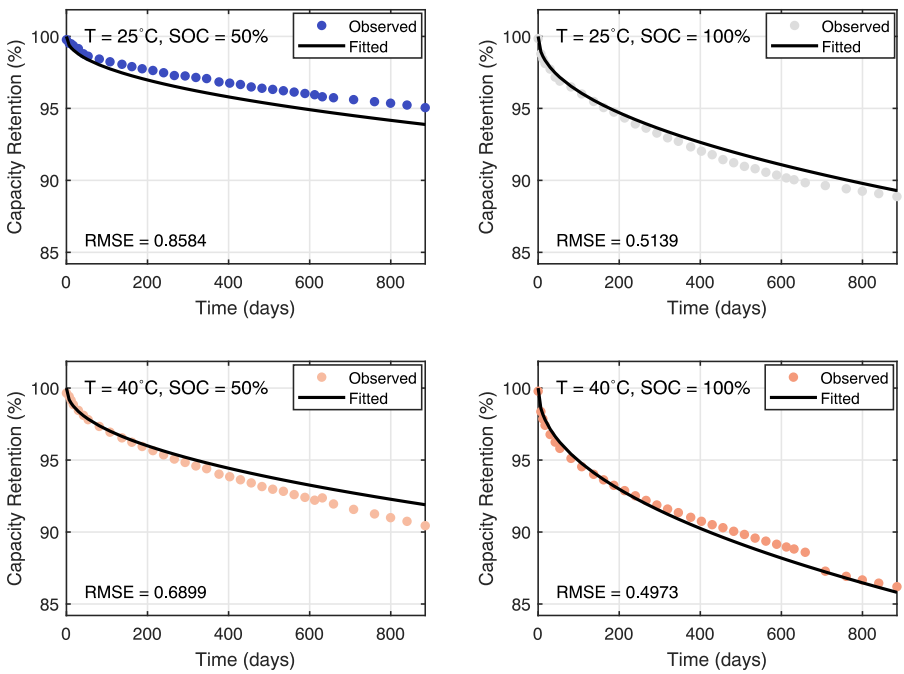

Figure 6.3: Measured and model-predicted calendar ageing of a 2.85 Ah LFP cell under different temperatures and SOC.

6.3.2 Cycling Ageing: Validation and Parameter Analysis

The cycling ageing model 6.3 was fitted to all 11 experimental degradation data shown in figure 6.2. Overall, the model captures the combined influence of temperature, C-rate, SOC window, and mean SOC, and reflects the main degradation behaiour observed in the data.

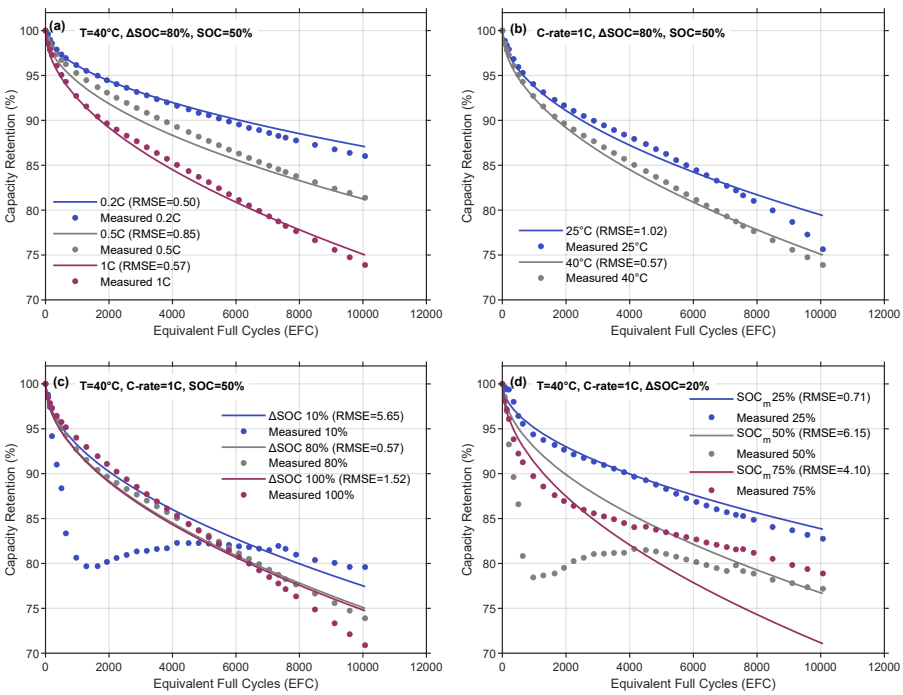

Figure 6.4: Measured and model-predicted cycling ageing of a 2.85 Ah LFP cell. 2.3.4.

Figure 6.4 compares the measured capacity retention with the corresponding model predictions. As expected, cycling at higher temperatures, using larger SOC windows, operating at higher C-rates, and maintaining higher mean SOC levels all lead to faster capacity retention. The model provides a good representation of these behaviours across most test conditions. Two cases however, the 10% SOC window in (c) and the lowest mean SOC condition in (d) show slight capacity increases in the experimental data, which the model

cannot reproduce. The recorded behaviour at this low SOC condition cannot be captured well by the selected model. (a) highlights the effect of cycling rate. The fitted exponent is $b = 0.40$, and the model reaches RMSE values of 0.50, 0.85, and 0.57 for 0.2C, 0.5C, and 1C, respectively. These results indicate that the model reliably captures the increase in degradation with higher C-rates. The temperature effect, shown in (b), give an activation energy of $E_a = 10.05\text{kJ}\,\text{mol}^{-1}$. As commonly observed for LFP cells, cycling at 40°C causes faster capacity loss than at 25°C. The influence of SOC window is shown in (c) with an estimated exponent of $\alpha = 0.17$. RMSE values range from 5.65 to 0.57 across the different SOC amplitudes. Apart from the irregular 10% window case, the model correctly reproduces the expected behaviour of increasing degradation for deeper cycles. (d) shows the effect of mean SOC, for which the fitted exponent is $m = 0.29$. RMSE values vary between 6.15 and 0.71, with the best agreement obtained at a mean SOC of 25%.

Across all test conditions, the fitted pre-exponential factor is A=0.89. Overall, the identified parameters show that the model can represent the ageing behaviour over a wide range of operating conditions. The remaining deviations appear to be related mainly to irregularities in a few of the experimental datasets rather than limitation in the model itself. The calibrated parameters of the calendar and cycling ageing models are summarized in table 6.1.

Table 6.1: Calendar and cycling ageing model parameters used in (6.1) and (6.3)

Calendar	**Value**	**Cycling**	**Value**
A_{cal}	0.46	A_{cyc}	0.8914
$E_{a,\text{cal}}$	14221.59	a	0.1731
α	0.8628	m	0.2886
n	0.4932	b	0.3979
		z	0.5758
		$E_{a,\text{cyc}}$	10000

CHAPTER 7

Analysis of BESS operation

7.1 Controller and Performance Model

The controller used in this study is shown in Figure 7.1 and is based on the FCR activation droop and the EMS described in section 2.3. It takes the measured grid frequency as its input and determines the corresponding power request using the droop characteristics defined for FCR-N, FCR-D down, and FCR-D up (2.2, 2.4, 2.3). In this way, the BESS adjusts its output directly in response to deviations from the nominal grid frequency, which allow to fulfill the technical requirements of FCR services. Once the required power is calculated, a possible adjustment is done in order to remain within the operating limits of the battery to ensure that the delivered power remains consistent with the technical capabilities of the system. The delivered power is supplied to the grid and is also used as input to the SOC estimation part of the model, as shown in figure 7.1.

The SOC is continuously estimated to ensure that the BESS operates within the 0.1–0.9 range. Due to the flat voltage plateau characteristic of LFP chemistry, which limits the usefulness of voltage-based energy estimation, SOC and SOE are fairly equivalent within this operating range, as illustrated in

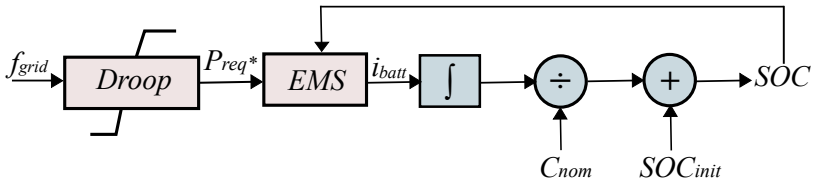

Figure 7.1: Block diagram of the FCR controller with SOC estimation

the figure.7.2.

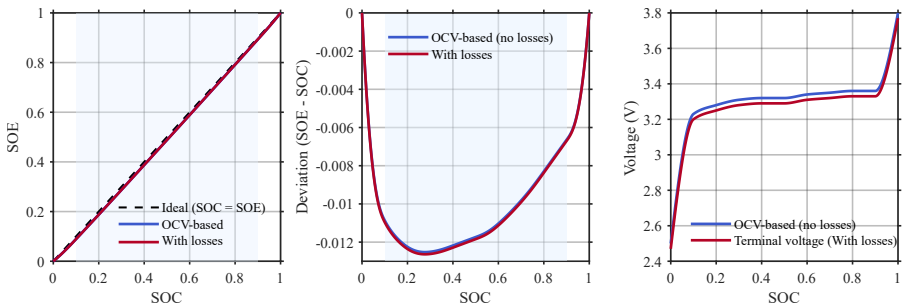

Figure 7.2: SOC, SOE, and OCV Characteristics of an LFP Cell.

The SOC estimation is important for identifying when additional energy management interventions are required. NEM and AEM, introduced in section 2.3.4, are activated directly based on the SOE. NEM follows the logic defined in 2.5 2.9, adding a small corrective charging or discharging power when the SOC approaches its predefined limits. AEM follows the conditions defined in 2.10,2.13, reducing the FCR response when the SOE moves outside the acceptable range and allowing the system to recover energy. By linking the droop-based power request (2.2-2.4) and the NEM/AEM states (2.5-2.13), this performance model shows how a BESS is providing FCR. It represents both the quick power response to frequency changes and the energy balancing state needed to keep the system operating over time.

7.2 Application of Battery Ageing Models under Dynamic Conditions

Battery degradation is evaluated by combining the calendar and cycling ageing approach described in Chapter 6 to estimate degradation over a full year of FCR operation under dynamic conditions, SOC and current are used as inputs to the model.

7.2.1 Calendar ageing under dynamic conditions

In this work, the calendar ageing model in (6.1) was used. However, during FCR operation the SOC varies continuously, and therefore this model (6.1) can not be applied directly. To represent dynamic operation, the model was converted into an incremental formulation by differentiation with respect to time

$$\frac{dQ_{\text{cal}}}{dt} = K_{\text{cal}} n \; SOC(t)^{\alpha} t^{n-1}. \tag{7.1}$$

Equation (7.1) describes the instantaneous calendar degradation rate as a function of the current SOC and accumulated storage time. For numerical implementation, the degradation increment over a discrete timestep Δt is evaluated as

$$\Delta Q_{\text{cal},k} = K_{\text{cal}} n SOC_k^{\alpha} t_k^{n-1} \Delta t \tag{7.2}$$

where SOC_k is the measured SOC at time t_k. The total calendar capacity loss is then obtained by

$$Q_{\text{cal}}(t_k) = \sum_{i=1}^{k} \Delta Q_{\text{cal},i} \tag{7.3}$$

7.2.2 Cycling Ageing under dynamic conditions

Cycling ageing is evaluated using rainflow counting algorithm, that is applied to the SOC profile from each FCR service. Following the rainflow procedure, the SOC profile is analyzed to obtain the cycle range ΔSOC and SOC_m for each identified cycle. After performing the rainflow procedure, a deadband filter was applied to suppress minor SOC fluctuations that do not contribute

meaningfully to battery ageing based on experimental observations showing that SOC range below approximately 2% have negligible degradation impact [52].

The cycling ageing model used in this work was originally calibrated under constant cycling conditions and expressed as a function of EFC as described in (6.3). However, during FCR operaton the battery experiences irregular cycling with continuously varying cycle range, mean SOC, and current profiles. Consequently, the (6.3) can not be applied directly. To represent this dynamic behaviour, the model was reformulated into an incremental form by differentiation with respect to N, which is the total EFC

$$\frac{dQ_{\text{cyc}}}{dN} = K_{\text{cyc}}(\Delta SOC)^a SOC_m^m C^b z N^{z-1}. \tag{7.4}$$

For each identified cycle i, the corresponding degradation increment was evaluated as

$$\Delta Q_{\text{cyc},i} = K_{\text{cyc}} \Delta SOC_i^a SOC_{m,i}^m C_i^b z N_i^{z-1} \Delta N_i \tag{7.5}$$

where ΔN_i is the fractional EFC contribution associated with each detected cycle. The accumulated EFC are calculated by cumulatively summing the rainflow derived SOC range and devided by twice the usable SOC window, as one full cycle consists of two half-cycles. The mean C-rate C_i was computed as the average absolute battery current divided by nominal battery capacity over the corresponding cycle interval. Due to rapid current variations during FCR operation, the calculated C-rate was filtered using a low-pass filter on order to remove fast oscillations.

Total cycling degradation was then obtained by cumulative summation of all incremental contributions following

$$Q_{\text{cyc}} = \sum_{i=1}^{N} \Delta Q_{\text{cyc},i} \tag{7.6}$$

7.2.3 Total Degradation Estimation

Total capacity loss was obtained by additively combining independent calendar and cycling degradation contributions

$$Q_{\text{total}} = Q_{\text{cal}} + Q_{\text{cyc}}. \tag{7.7}$$

The incremental calendar and cycling ageing formulations allow degradation to be evaluated under dynamic FCR conditions. Figure 7.3 summarises the overall modelling approach, from model parameterisation to application under dynamic operation.

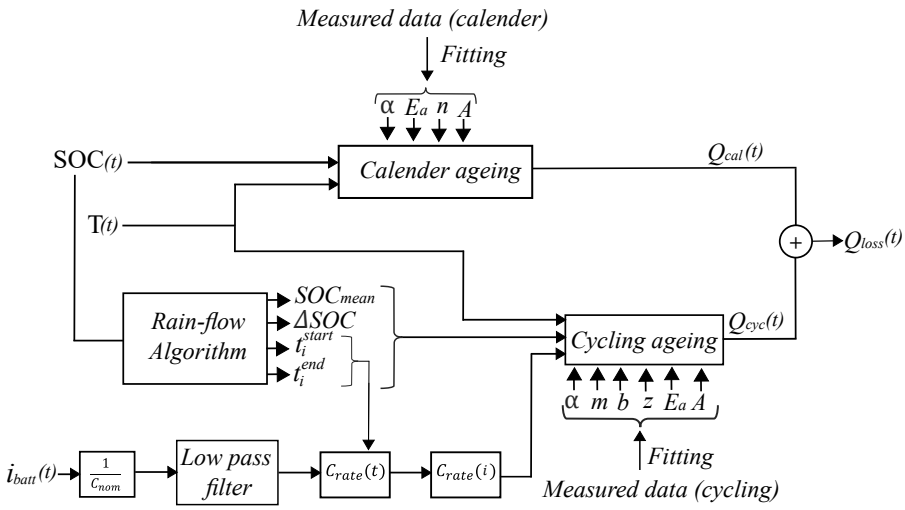

Figure 7.3: Overview of the ageing model structure combining rainflow cycle extraction, calendar ageing, and cycling ageing.

7.3 Economic Analysis procedure

The economic model described in Section 3.5 is utilized in this section. The analysis considers both calendar and cycling degradation costs. The FCR remuneration price is obtained from the year 2024, Figure 7.4 presents the FCR capacity remuneration for 2024, illustrating the variation in remuneration price for providing FCR services. The economic parameters used for the BESS are summarized in Table 7.1.

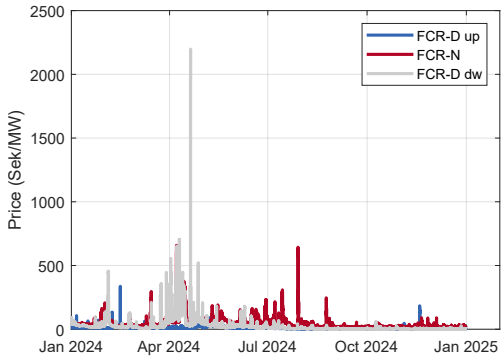

Figure 7.4: FCR capacity remuneration (2024). 2.3.4.

Table 7.1: Economic parameters used for the battery energy storage system (BESS).

Parameter	**Symbol**	**Value**
Battery replacement cost	C^{REP}	108 k€ / MW
Interest rate	i	5%
Extra cost	i	25%
Operation and maintenance cost	C^{OM}	2%
Battery lifetime	L	10 years
End-of-life capacity threshold	EOL	80%
Salvage value ratio	r^{SV}	0.5

The total profit of the battery system providing FCR services is then calculated using 3.15, which accounts for market revenue and the degradation-related costs from both calendar and cycling ageing.

CHAPTER 8

Operation of BESS for grid services

8.1 Input Data

Figure 8.1 presents the grid frequency profile for 2022 used in this work. For most of the year, the frequency remains close to the nominal value of 50 Hz, which indicate stable system. The frequency consists of small, continuous deviations, which reflect normal power imbalances that are typically corrected by FCR-N service. Larger frequency deviations occur occasionally. Overall, the frequency profile shows that FCR operation is dominated by frequent small responses around the nominal frequency, with only a few larger deviations.

8.2 BESS Operational Response under single FCR Services

8.2.1 FCR-N Regulation: Power and SOE Behaviour

Figure 8.2 shows the BESS power response and the corresponding SOE during FCR-N provision for one year. The power profile in Fig.(a) is concentrated

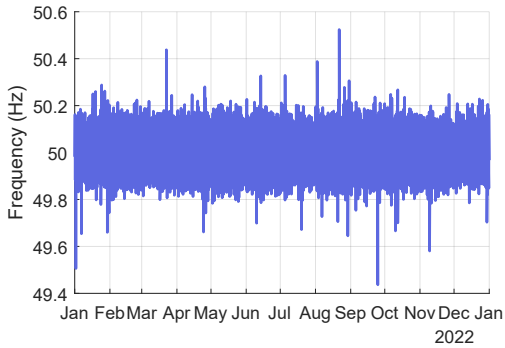

Figure 8.1: Grid frequency profile over one year (2022)

around zero and shows frequent bidirectional fluctuations, which reflect the symmetric activation of FCR-N in response to grid frequency. Even thought the contracted FCR-N capacity is 0.5 MW, power values goeing up to 0.67 MW are observed. This is due to the additional 34% reserve capacity allocated for NEM.

The SOE in Fig. (b) remains within the defined operational limits (0.1-0.9) throughout the entire period.

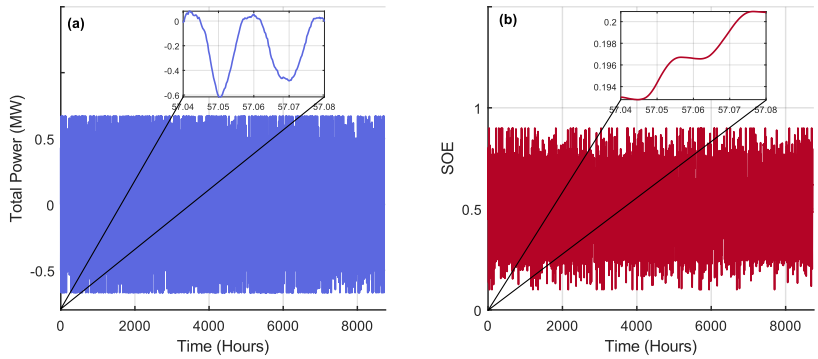

Figure 8.2: System Response to provide FCR-N, (a) Power and (b) SOE.

8.2.2 FCR-D Up Regulation: Power and SOE Behaviour

Figure 8.3 shows the BESS power response and the corresponding SOE during FCR-D up. Even thought FCR-D up is designed to inject power to the grid, the power profile in Fig.(a) shows negative power values. This occurs because, under normal system conditions, when the frequency remains within the deadband of 49.9–50.1 Hz, the NEM state is activated as the SOE within the NEM activation. In this case, the battery absorbs power from the grid to restore SOE.

As a result, the SOE in Fig. (b) remains at relatively high levels for most of the period, with only small decreases during FCR-D Up activation events. This figure shows that NEM state can recover the energy lost when providing FCR-D Up.

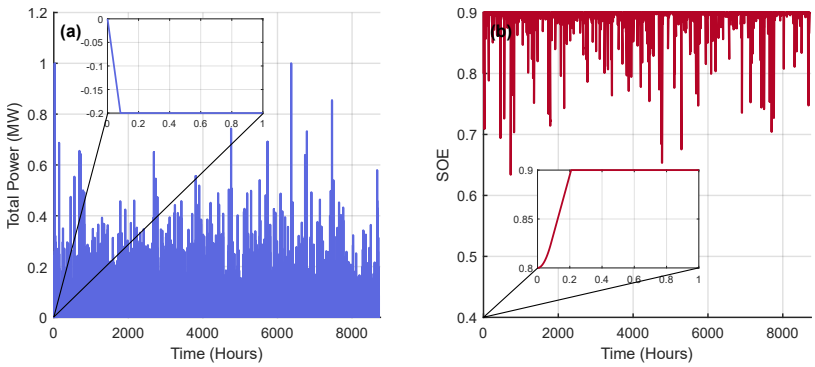

Figure 8.3: System Response to provide FCR-D up, (a) Power and (b) SOE.

8.2.3 FCR-D Down Regulation: Power and SOE Behaviour

Figure 8.4 shows the BESS power response and the corresponding SOE during FCR-D Down. Although FCR-D Down is designed to absorb power from the grid, the power profile in Fig. (a) shows mainly positive power values. The reason is that, under normal system conditions, when the frequency remains within the deadband of 49.9–50.1 Hz, the NEM state is activated based on the SOE level. In this case, the battery injects power to the grid to prevent excessive energy accumulation.

As a result, the SOE in fig. (b) remains at low levels for most of the period, with only short increases during FCR-D Down activation events. This figure shows that NEM operation can reduce the excess energy gained during FCR-D Down. Therefore, the battery cycling behavior differs from pure FCR-D Down operation.

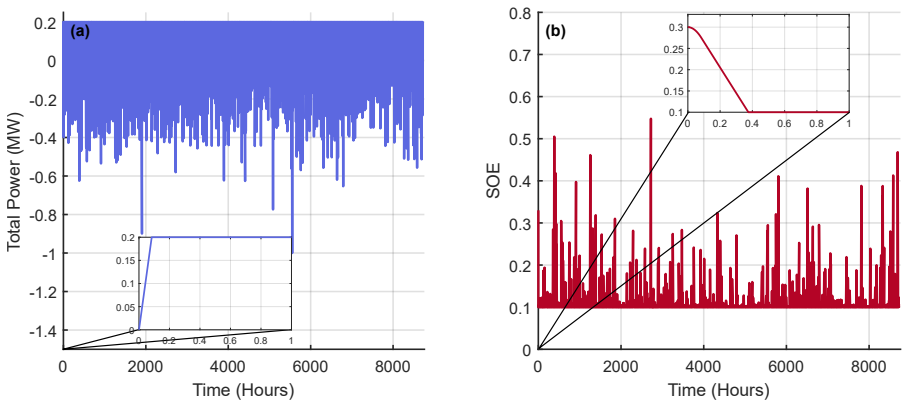

Figure 8.4: System Response to provide FCR-D down, (a) Power and (b) SOE.

8.3 Battery Ageing under FCR Operation

8.3.1 Calendar and Cycling Degradation Comparison

Figure 8.5 illustrates the calendar and cycling capacity loss under FCR-N, FCR-D up, and FCR-D down operation over one year. The results show that FCR-D up has the highest calendar capacity loss of 6.3% after one year and this is due to the high SOC as shown in Figure 8.3, followed by FCR-N about 3.7%, while FCR-D down has minimal degradation, remaining below 0.96% and the reason being that the battery stays at low SOC for the major part of the operating period.

This behavior is attributed to differences in SOC, where higher SOC levels in FCR-D up accelerate calendar ageing. On the other hand, lower SOC levels in FCR-D down has less impact on calendar ageing.

In contrast, cycling ageing is most significant under FCR-N, reaching 1.1% capacity loss after about 450 EFCs due to continuous bidirectional activation.

FCR-D up has low cycling degradation of around 0.17% after 21 EFCs over one year, almost the same for FCR-D down with a capacity loss around 0.14% even after 28 EFCs and this is due to low SOC level of this service.

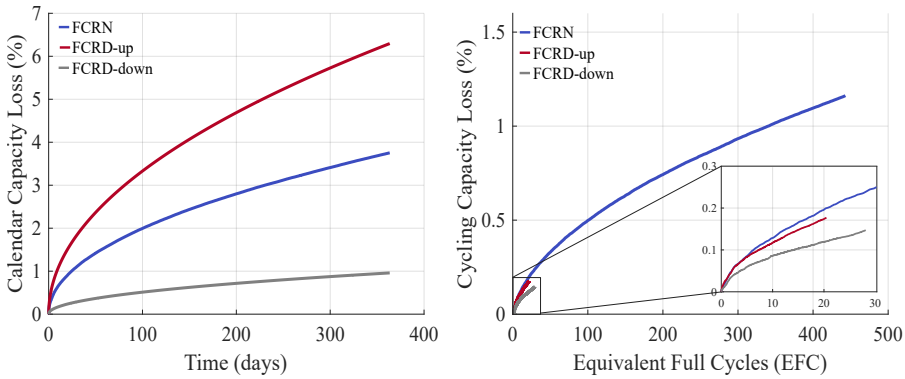

Figure 8.5: Calender and cycling Capacity loss of the battery under FCR-N, FCR-D up, and FCR-D down operation over one year .

8.3.2 Contribution of Calendar vs Cycling Ageing

Figure 8.6 presents the contributions of calendar and cycling ageing to the total capacity loss for each FCR service. For FCR-D up, calendar ageing accounts for 85% of the total degradation (6.4%), indicating that high SOC is the dominant stress factor. FCR-N is mainly driven by calender ageing as well, which contributes with 75% of the total capacity loss (4.9%), while cycling ageing accounts for 1.2%, due to continuous bidirectional activation and higher equivalent full cycles. FCR-D down remains weakly affected for both calender and cycle ageing, with calendar ageing contributing 83% of the total loss (1.1%), confirming that low SOC operation results in limited battery stress.

8.3.3 SOC Distribution

Figure 8.7 illustrates the distribution of mean SOC as a function of ΔSOC for the three FCR services, together with the corresponding cycle count density. In Fig.8.7(a), FCR-N has high cycle count density concentrated at mean SOC

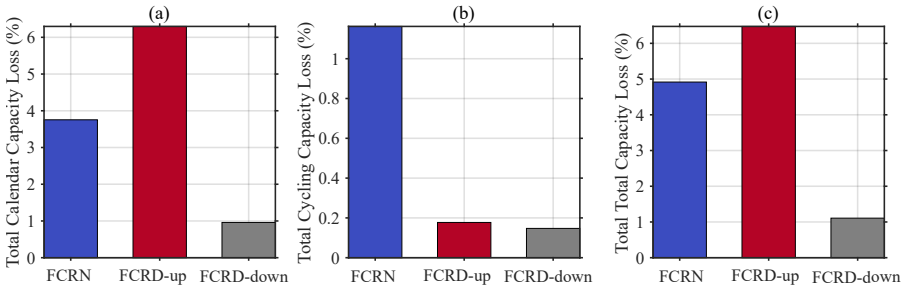

Figure 8.6: Breakdown of capacity degradation under FCR-N, FCR-D up, and FCR-D down operation: (a) total calendar capacity loss, (b) total cycling capacity loss, and (c) total capacity loss over one year.

values between 0.2 and 0.8 with ΔSOC below 0.05, indicating the presence of micro-cycles. In Fig.8.7 (b), FCR-D up operates mainly at high mean SOC levels (0.65–0.9) with small ΔSOC, corresponding to micro-cycling around high SOC. In Fig.8.7(c), FCR-D down is concentrated at low mean SOC values (0.1–0.55) with moderate ΔSOC liss than 0.5. Overall, for all services, the majority of cycles occur at ΔSOC below 0.05, confirming the dominance of micro-cycles in FCR operation.

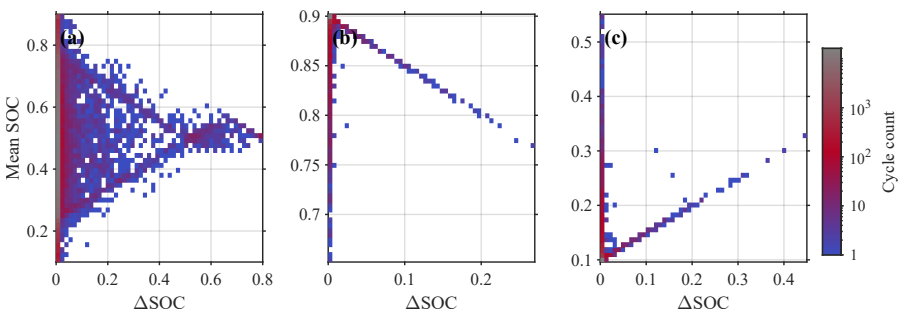

Figure 8.7: Relationship between mean SOC and SOC variation (ΔSOC) under FCR operation.

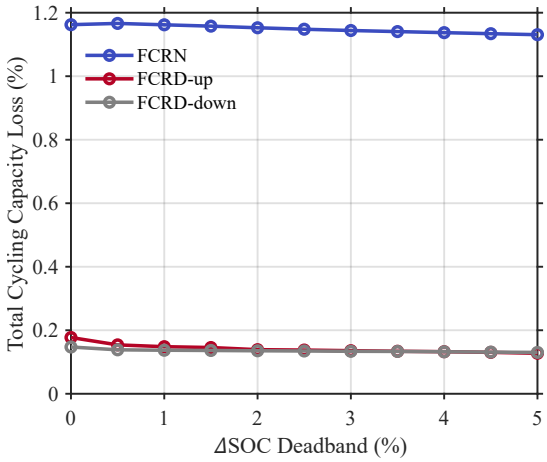

Figure 8.8: Sensitivity of Cycling Degradation to ΔSOC deadband Filtering.

8.3.4 Impact of SOC Deadband on Cycling Ageing

Figure 8.8 illustrates the effect of SOC range deadband, implemented as a filtering that suppresses microcycles below a specified amplitude, on total cycling capacity loss. For FCR-N, increasing the deadband from 0% to 5% results in only a negligible reduction in annual capacity loss (from 1.16% to 1.13%). This indicates that, even thought the deadband suppresses some high-frequency micro-cycling, these cycles contribute little to overall battery degradation. For FCR-D-up and FCR-D-down, total capacity loss is much lower than for FCR-N, remaining below 0.2% across all deadband values. In the FCR-D-up, capacity loss decreases from about 0.17% at 0% deadband to 0.13% at 5%, while for FCR-D-down the reduction is smaller, from 0.14% to 0.13%. Although both services show reduced degradation, the effect is small due to the largely unidirectional nature of FCR-D. Because FCR-D primarily responds to large disturbances, micro-cycling is much less pronounced than in FCR-N.

The results show that battery degradation during FCR operation is mainly determined by the SOC operating conditions of each service.

8.3.5 Discussion: Impact of FCR Services on SOC Profiles and Degradation Behaviour

The degradation behaviour observed for the three different FCR services can be interpreted using the calendar and cycling ageing models introduced in Chapter 6. Even thought all services are driven by the same grid frequency profile, each FCR service operates over a distinct frequency range, as defined in (2.2), (2.4), and (2.3). Consequently, each service has a different power response and SOC profile. These SOC profiles lead to different ageing behaviour.

For FCR-D up, the battery remains at high SOC for most of the operating time, as shown in Fig.8.3 and Fig. 8.7 (b). The calendar ageing model in 6.1 shows a strong dependency on SOC, with a fitted exponent $\alpha = 0.863$. This value which is extracted from the experimental storage data, where cells stored at 100% SOC degraded much faster than those stored at 50% SOC. As results, high SOC values during FCR-D up leads to high calendar ageing, which accounts for 85% of the total capacity loss. High SOC increases electrode potential and accelerates parasitic reactions, such as electrolyte decomposition and lithium consumption, which are captured by the SOC and temperature terms of the calendar ageing model [53].

FCR-N on the other is characterised by continuous bidirectional power activation, with the SOC varies around 50% SOC. This service gives 450 EFCs for one year with the existence of micro-cycles (Fig.8.7(a)). For FCR-N, calendar ageing remains dominant relative to cycling ageing. However, the cycling ageing under FCR-N is higher than that for FCR-D up and FCR-D down. This difference arises from the operational nature of FCR-N, which requires continuous response to small frequency deviations, whereas FCR-D services are activated primarily during larger frequency diviations. The cycling ageing model in (6.3) incorporates SOC swing, mean SOC, and accumulated EFC with the fitted exponents $a = 0.17$, $m = 0.29$, and $z = 0.58$, indicate that degradation is mainly driven by EFC and SOC. Consequently, the bidirectional regulation and frequent SOC oscillations during FCR-N cause electrochemical and mechanical stress on the electrode which lead to higher capacity loss.

FCR-D down shows a different operating pattern compared to the other services. The SOC remains mainly at low levels, as shown in Fig8.4 and Fig.8.7(c). According to the calendar ageing model, operation at low SOC

results in significantly lower degradation due to the strong SOC dependence. At the same time, FCR-D down is not needed as FCR-N leading to a low EFCs. Consequently, both calendar and cycling ageing remain small, which explains the minimal capacity loss observed for FCR-D down.

The SOC deadband analysis aligned with these results. Although increasing the deadband reduces small SOC fluctuations, it slightly decreases cycling degradation. This indicates that degradation is driven mainly by the large SOC range Fig.8.8.

Considering the strong impact of high SOC on degradation, Figure8.9 illustrates the impact of reducing the upper SOC limit of FCR-D up from 0.9 to 0.7 on calendar ageing. By limiting the maximum SOC, the battery operates within a lower SOC range, avoiding prolonged exposure to high SOC conditions.

As a result, the annual calendar capacity loss decreases from 6.3% to 5.0%, corresponding to an absolute reduction of 1.3%. This improvement is attributed to the strong dependence of calendar ageing on SOC, where higher SOC levels accelerate degradation.

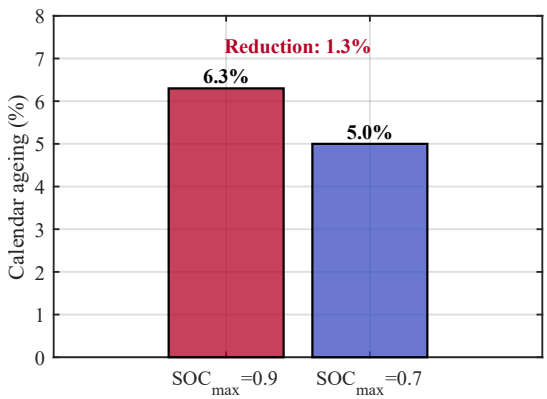

Figure 8.9: Impact of reducing the upper SOC limit on calendar ageing.

To evaluate how the different services impact ageing over the long, Fig. 8.10. FCR-D up reaches the 80% EOL after 9.95 years. indicating the highest degradation among the services. However, reducing the upper SOC limit for FCR-D up increases the battery lifetime, with the capacity reaching 84% In contrast, after 10 years of operation, the remaining capacity is 94% for FCR-

D down and 84% for FCR-N. These results confirm that FCR-D up shows higher ageing stress, while FCR-N and FCR-D down exhibit comparatively lower degradation.

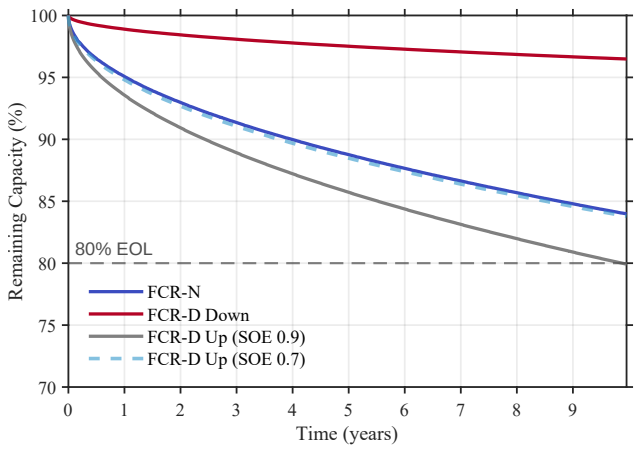

Figure 8.10: Battery degradation under different FCR services for a duration of 10 years.

8.4 BESS Operational Response under Combined FCR Services

In addition to single service operation, the battery can provide multiple FCR services simultaneously. Two configurations are considered: (i) combined FCR-D (FCR-D up and FCR-D down), where each service represents 50% of the total reserved capacity, and (ii) combined FCR-N with FCR-D, where FCR-N accounts for approximately 28% and FCR-D upp and ned each account for approximately 36% of the total reserved capacity..

8.4.1 SOE Behaviour under Combined Services

Figure 8.11 compares the SOE profile for an example fulfilling combined FCR services. The FCR-N with FCR-D configuration causes more SOE fluctuations as FCR-N is a symmetric service that requires both charging and discharging.

Even with these fluctuations, the SOE stays within the operational limits (0.1–0.9). In comparison, providing FCR-D up and FCR-D down together results in a smoother SOE profile with small fluctuations. However, an increase in SOE is observed over time, indicating more charging than discharging.

This behaviour is explained by frequency distribution in Fig. 8.12, where $f > 50.1$ Hz (1.02%) occurs more often than $f < 49.9$ Hz (0.81%). As a result, downward regulation is activated more frequently, which lead to battery charging and an increase in SOE.

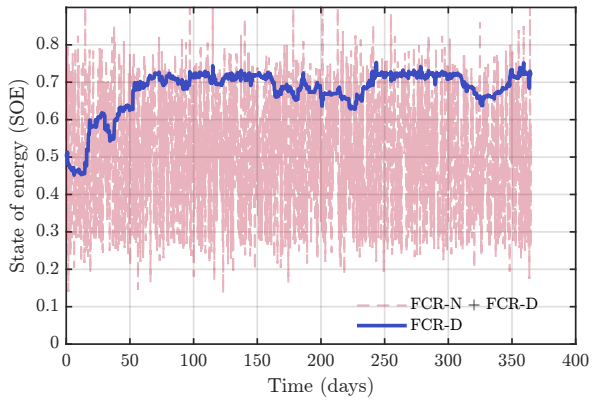

Figure 8.11: SOE evolution under combined FCR services: comparison of FCR-D up/down and FCR-N with FCR-D operation.

8.4.2 Calendar Ageing under Combined Services

Figure 8.13 shows the calendar degradation for the combined services. FCR-N with FCR-D leads to a capacity loss of 3.7% after one year, while FCR-D (up and down) results in 4.6%. This difference is attributed to the SOC profile Figure 8.11. The inclusion of FCR-N causes continuous fluctuations around mid SOC, limiting the operation at high SOC levels. In contrast, FCR-D maintains a higher average SOC, which accelerates calendar ageing.

8.4.3 Cycling Ageing under Combined Services

Figure 8.14 shows the cycling degradation as a function of equivalent full cycles for the combined services. For FCR-D, the cycling capacity loss remains close

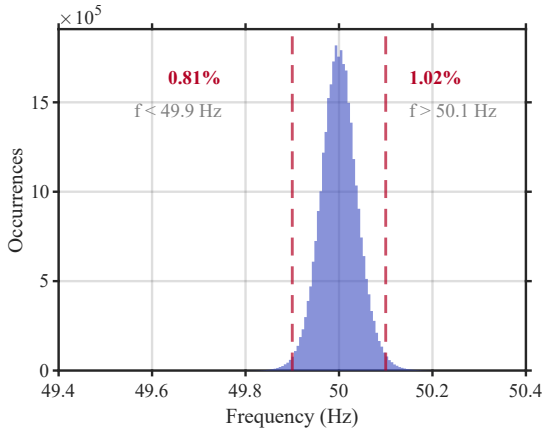

Figure 8.12: Grid frequency distribution.

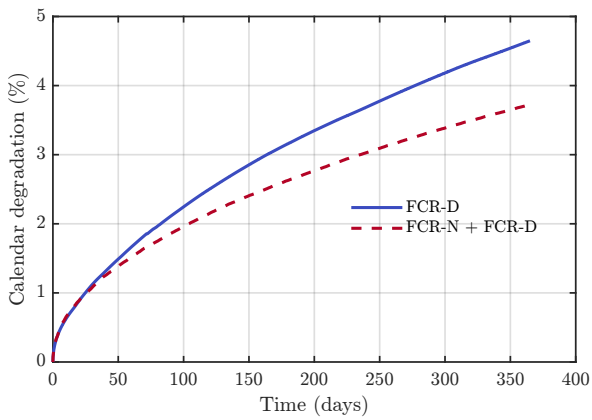

Figure 8.13: Calendar degradation under combined FCR services.

to 0% after 2 EFC over one year.

In contrast, for the combination of FCR-N and FCR-D, the cycling degradation is higher, reaching 0.52% after 200 EFC. This is because the battery operates continuously when providing FCR-N.

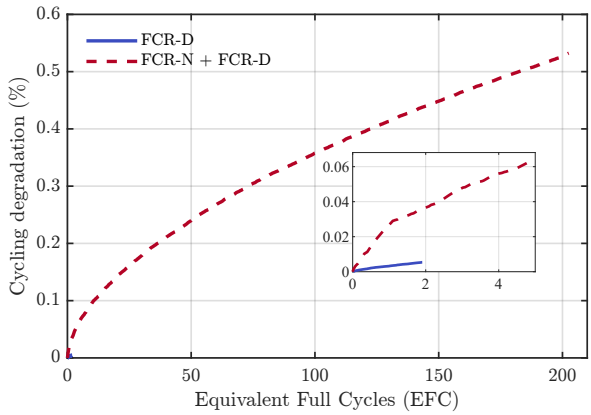

Figure 8.14: Cycling degradation as a function of equivalent full cycles under combined FCR services.

8.4.4 Discussion: Combined Service Provision

The results show that combining FCR services changes the battery behaviour. For the combined case of FCR-D up and FCR-D down, the SOC stays within a narrower range compared to single service operation. The battery does not operate at very high or very low SOE levels. However, the SOC shifts toward higher values over time. This is because downward regulation is activated more often than upward regulation. As a result, the battery charges more than it discharges over time, which increases the SOE.

This higher SOC leads to more calendar ageing compared to the case with only FCR-D down, but it is still lower than in the case with only FCR-D up. In addition, the battery shows limited cycling, even though both upward and downward regulation are present. This is because the operation is not balanced, and one direction is activated more often than the other. Therefore, the number of equivalent full cycles remains low.

The obtained number of EFC is 2 over one year. This low value is consistent

with the total energy throughput. In this case, the total exchanged energy is about 5 MWh. For a battery with a capacity of 1 MWh, this gives 2.5 EFCS which is close to the rainflow-based result.

The low EFC is explained by the nature of FCR operation. The battery mainly performs small and fast power changes, which lead to small SOC variations instead of full charge and discharge cycles. Therefore, many small changes only result in a few EFC.

For comparison, the standalone operation of FCR-D up and FCR-D down gives higher cycling, with 20 and 28 cycles per year, respectively. This is mainly due to the activation of NEM. During standalone operation, NEM brings the SOC back to its reference limits (0.9 for FCR-D up and 0.1 for FCR-D down). This repeated recovery adds extra charge and discharge actions, which increases the number of cycles.

In contrast, in the combined operation, the SOC does not reach the limits needed to activate NEM. As a result, the battery mainly operates with FCR-D only, without frequent recovery actions. This reduces large SOC changes and leads to a much lower number of EFC.

When FCR-N is combined with FCR-D, the SOC behaviour changes clearly. The SOC moves up and down continuously because FCR-N operates in both directions. It stays around medium values instead of being close to the upper or lower limits.

This leads to more charge and discharge actions, which increases cycling ageing. At the same time, the battery operates for shorter durations at high SOC, which reduces calendar ageing compared to the combined FCR-D case.

Overall, the main ageing mechanism depends on the service combination.

8.5 Economic Performance of Battery Participation in Reserve Markets

Figure 8.15 presents the revenue and net profit for different FCR service configurations using 2025 market prices. Looking first at the individual services, both FCR Up and FCR Down show relatively limited economic performance. Both services have similar revenues (0.53 MSEK and 0.52 MSEK), while their net profits are 0.35 MSEK and 0.49 MSEK, which reflect differences in ageing costs. FCR Up has lower net profit despite similar revenue, indicating higher degradation compared to FCR Down.

When the two are combined into FCR-D, the results improve. Revenue increases to 0.87 MSEK and net profit to 0.74 MSEK, which demonstrate that providing upward and downward regulation together is more advantageous than offering them separately.

FCR-N show higher performance, with 1.18 MSEK in revenue and 1.04 MSEK in net profit. The best service results are observed for the combined FCR-N+D configuration, which achieves 1.22 MSEK in revenue and 1.10 MSEK in net profit.

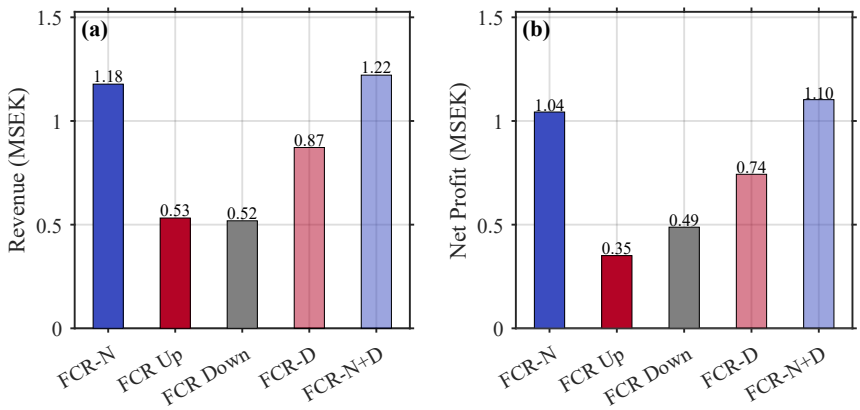

Figure 8.15: Comparison of total revenue and net profit for standalone FCR services (FCR-N, FCR Up, FCR Down) and the combined FCR-N+D and FCR-D configurations.

Figure 8.16 presents the cash flow for the different FCR service configurations over the project lifetime. All cases have an initial negative cash flow due to the investment cost of 1.2 MSEK, followed by positive cash flows during the operational years. It is assumed that revenue decreases by 10% over time due to market saturation effects. This reduction is reflected in the gradual decline in cash flow in later years for all configurations. Among the individual services, FCR Up and FCR Down generate low annual cash flows, 0.50 MSEK for FCR-D Up and 0.49 MSEK for FCR-D Down, consistent with their lower revenue. The combined FCR-D configuration shows a higher cash flow (0.84 MSEK), reflecting the benefit of providing both upward and downward regulation simultaneously.

FCR-N has higher annual cash flows compared to the individual FCR-D

services (1.15 MSEK), while the combined FCR-N+D configuration achieves the highest cash flow of 1.19 MSEK. This confirms that providing multiple services leads to greater cash generation over time.

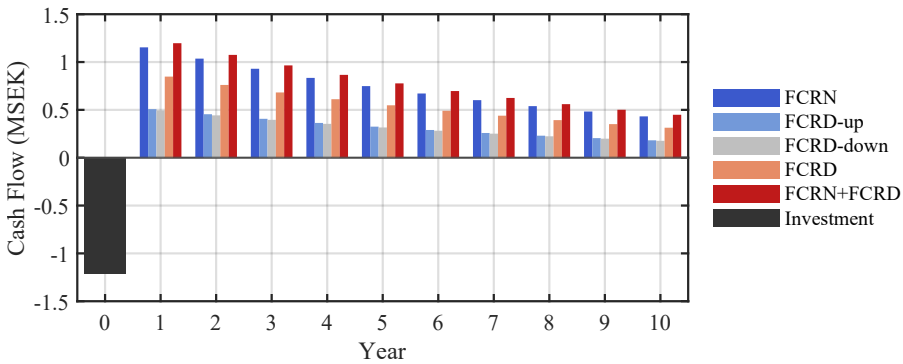

Figure 8.16: Cash flow over the project lifetime for different FCR service configurations.

Figure 8.17 presents the payback period for different FCR service configurations. FCRN, FCRD, and the combined FCRN+FCRD configuration have the shortest payback time of 2 years. In contrast, FCRD-up and FCRD-down have longer payback periods about 3 years,

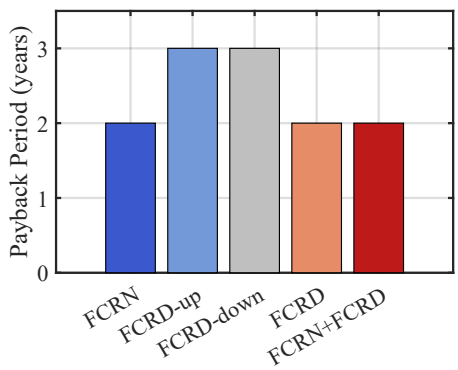

Figure 8.17: Comparison of payback periods for different FCR service configurations

Figure 8.18 shows how the payback period changes as the remuneration price decreases. As the remuneration decreases, all cases show an increase in payback period, but not at the same rate. FCRD-up and FCRD-down are more affected, increasing from 3 years to around 9 to 10 years at high reductions (70%). In comparison, FCRN, FCRD, and FCRN+FCRD increase from 2 years to around 4–6 years over the same range.

Overall, while reduction of 50% still allow for acceptable payback periods, larger reductions lead to long recovery times and reduced economic viability. Figure 8.19 presents the payback period when the remuneration price is re-

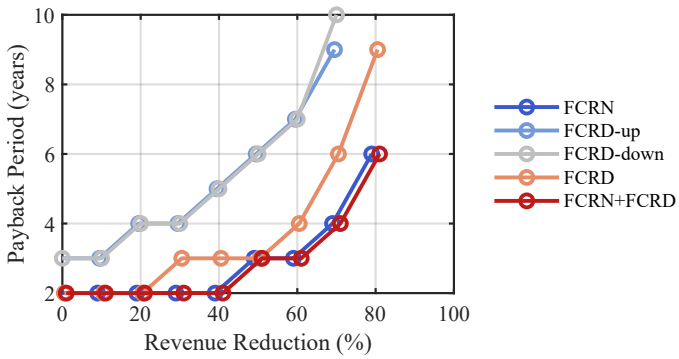

Figure 8.18: Sensitivity analysis of payback period under decreasing remuneration levels for different FCR service configurations.

duced by 50% and the battery cost increases from 108 $/kWh to 151 $/kWh, reflecting the price increase observed in 2022 during the Russia–Ukraine conflict Figure 1.1.

When the battery cost increases to 151 $/kWh, the payback period increases across all cases. FCRN rise to 4 years, while FCRD increases to 5 years. The largest impact is observed for FCRD-up and FCRD-down, which increase to 8 years.

This shows that higher investment cost significantly affects the payback period, especially for directional services. Despite this increase, most configurations still remain within a moderate payback range, although their economic attractiveness is reduced compared to the base case.

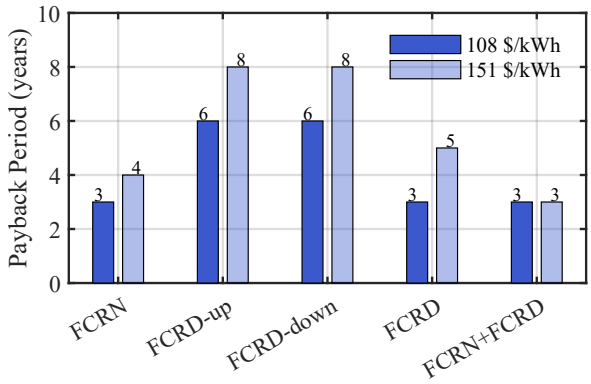

Figure 8.19: Payback period under 50% remuneration reduction for two battery cost levels (108 and 151 $/kWh).

8.5.1 Discussion: Economic Performance of Battery Participation in Reserve Markets

The results show that the economic performance of battery participation in reserve markets depends strongly on how the services are combined. Providing a single service, particularly directional FCR-D (up or down), leads to lower profitability and longer payback period. In contrast, combining services improves the utilization of the battery and results in more stable and higher returns.

Another important observation is the sensitivity to market conditions. The analysis shows that moderate reductions in remuneration (around 50%) can still maintain acceptable payback periods. However, larger reductions significantly weaken the economic case, as longer recovery times increase investment risk.

In addition to market uncertainty, investment cost plays a key role. The increase in battery cost from 108 to 151 $/kWh, reflecting the price rise observed during the 2022 Russia–Ukraine war, further reduces economic attractiveness. This impact is more pronounced for less profitable configurations, while combined services remain relatively more robust.

Overall, the results suggest that both market price levels and capital costs are critical factors, and that combining multiple FCR services is an effective strategy to improve economic performance and reduce risk.

CHAPTER 9

Conclusion

This thesis evaluated the technical and economic performance of BESS providing FCR-N, FCR-D up, and FCR-D down services in the Nordic power system. A dynamic simulation combined with semi-empirical calendar and cycling ageing models was used to assess degradation and profitability under real operating conditions.

The results show that degradation is mainly determined by the SOC operating range of each service. FCR-D up exhibits the highest capacity loss (about 6.4% after one year), dominated by calendar ageing (85%) due to operation at high SOC. FCR-N results in a total capacity loss of around 4.9% and approximately 450 EFCs per year, leading to higher cycling degradation (about 1.2%) compared to other services. In contrast, FCR-D down shows the lowest degradation (around 1.1%) as it operates mainly at low SOC. The deadband analysis indicates that micro-cycles have only a minor effect on cycling ageing.

Economically, profitability depends on both degradation and market remuneration. Under 2025 conditions, the combined FCR-N+D configuration gives the highest net profit around 1.10 MSEK, followed by FCR-N with net profit of 1.04 MSEK and FCR-D 0.74 MSEK. In contrast, stand-alone FCR-D up and FCR-D down show lower profitability, with net profits of 0.35 MSEK and

0.49 MSEK, respectively.

These results indicate that combining services improves revenue generation and overall economic performance, while standalone directional services remain less attractive. Overall, the results show that the viability of BESS in FCR markets depends on the combined effect of SOC operation, ageing, and market conditions.

CHAPTER 10

Future Work

This study provides an assessment of degradation and economic performance for individual FCR services, further research could definitely improve the understanding of how BESS participate in ancillary service markets.

First, future research could combine FCR services with peak shaving in a V2G is an important direction for future research. Using EV may increase revenue, but can also increase degradation.

Second, experimental validation based on cycling tests focused on micro-cycles would be beneficial to validate the simulation results.

Third, an environmental comparison of NMC and LFP batteries, with and without V2G, is needed to assess sustainability using life-cycle analysis across different operating strategies.

Finally, alternative storage options, such as redox flow batteries, should be evaluated for FCR and other grid services by comparing response time, efficiency, and degradation with lithium-ion systems to determine their suitability for frequency control.

References

[1] European Commission, *Fit for 55*, 2021. [Online]. Available: https://ec.europa.eu/info/strategy/priorities-2019-2024/european-green-deal/delivering-european-green-deal_en.

[2] Energiföretagen Sverige. "Energiåret – årsstatistik." Accessed: 2026-04-09. [Online]. Available: https://www.energiforetagen.se/statistik/energiaret/.

[3] ENTSO-E, *Continental europe operation handbook*, 2019.

[4] D. Rose et al., "Battery storage for frequency services," *IEEE Transactions on Power Systems*, pp. 1678–1689, 2020.

[5] I. Staffell et al., "Cost projections for battery systems," *Joule*, pp. 789–812, 2022.

[6] BloombergNEF. "Lithium-ion battery pack prices fall to $108 per kilowatt-hour, despite rising metal prices." Accessed: 2026-02-17, Bloomberg New Energy Finance. [Online]. Available: https://about.bnef.com/insights/clean-transport/lithium-ion-battery-pack-prices-fall-to-108-per-kilowatt-hour-despite-rising-metal-prices-bloombergnef/.

[7] Fluence, *Nordic bess projects*, 2023. [Online]. Available: https://fluenceenergy.com/projects/nordics/.

[8] M. Świerczyński, A. Stroe, R. Teodorescu, and S. K. Kær, "Degradation in frequency containment reserve applications of lithium-ion batteries," *Journal of Energy Storage*, pp. 1–12, 2018.

[9] A. Maheshwari et al., "Economic impact of battery degradation," *Applied Energy*, pp. 116–128, 2021.

[10] Y. Hu, M. Armada, and M. Jesús Sánchez, "Potential utilization of battery energy storage systems (bess) in the major european electricity markets," *Applied Energy*, p. 119 512, 2022, ISSN: 0306-2619. [Online]. Available: https://www.sciencedirect.com/science/article/pii/S0306261922008340.

[11] N. Mirzaei Alavijeh, R. Khezri, M. Mazidi, D. Steen, and A. T. Le, "Profit benchmarking and degradation analysis for revenue stacking of batteries in sweden's day-ahead electricity and frequency containment reserve markets," *Applied Energy*, p. 125 151, 2025, ISSN: 0306-2619. [Online]. Available: https://www.sciencedirect.com/science/article/pii/S0306261924025352.

[12] M. Wesselmann, L. Wilkening, and T. A. Kern, "Techno-economic evaluation of single and multi-purpose grid-scale battery systems," *Journal of Energy Storage*, p. 101 790, 2020, ISSN: 2352-152X. [Online]. Available: https://www.sciencedirect.com/science/article/pii/S2352152X20316273.

[13] G. T. Giannakopoulos, D. A. Papadaskalopoulos, M. D. Karasavvidis, and P. N. Vovos, "Profitability analysis of battery energy storage in energy and balancing markets: A case study in the greek market," *Energies*, 2025, ISSN: 1996-1073. [Online]. Available: https://www.mdpi.com/1996-1073/18/4/911.

[14] M. Ahouad, A. Sunjaq, E. Wikner, and T. Thiringer, "Economic assessment of battery energy storage for frequency regulation in the nordic power systems," in *2024 20th International Conference on the European Energy Market (EEM)*, 2024, pp. 1–5.

[15] P. Astero and C. Evens, "Optimum operation of battery storage system in frequency containment reserves markets," *IEEE Transactions on Smart Grid*, pp. 4906–4915, 2020.

[16] K. Jacqué, L. Koltermann, J. Figgener, S. Zurmühlen, and D. U. Sauer, "The influence of frequency containment reserve on the operational data and the state of health of the hybrid stationary large-scale storage system," *Energies*, p. 1342, 2022.

[17] D. Gräf et al., "What drives capacity degradation in utility-scale battery energy storage systems? the impact of operating strategy and temperature in different grid applications," *Journal of Energy Storage*, p. 103 533, 2022, ISSN: 2352-152X. [Online]. Available: https://www.sciencedirect.com/science/article/pii/S2352152X21012147.

[18] H. Khajeh, C. Parthasarathy, and H. Laaksonen, "Effects of battery aging on bess participation in frequency service markets – finnish case study," in *2022 18th International Conference on the European Energy Market (EEM)*, 2022, pp. 1–6.

[19] A. J. Wood, B. F. Wollenberg, and G. B. Sheblé, *Power Generation, Operation, and Control*, 3rd. Wiley, 2013.

[20] European Union, *Commission regulation (eu) 2017/1485 of 2 august 2017 establishing a guideline on electricity transmission system operation*, Official Journal of the European Union, L 220, Accessed: 2025-10-26, Aug. 2017. [Online]. Available: https://eur-lex.europa.eu/legal-content/EN/TXT/?uri=CELEX:32017R1485.

[21] P. Kundur, *Power System Stability and Control*. New York: McGraw-Hill, 1994, ISBN: 978-0070359581.

[22] P. M. Anderson and A. A. Fouad, *Power System Control and Stability*, 2nd. New York, NY, USA: IEEE Press, 1990.

[23] P. Tielens, *Grid Dynamics and Control*. City: Publisher Name, 2016.

[24] J. Ullmark, L. Göransson, and F. Johnsson, "Frequency reserves and inertia in the transition to future electricity systems," *Energy Systems*, pp. 1527–1560, 2024.

[25] S. Bindu, L. Sigrist, and J. P. Chaves Ávila, "Frequency stability services to compensate for low inertia in renewable-dominated power systems," *Utilities Policy*, p. 101 938, 2025, ISSN: 0957-1787. [Online]. Available: https://www.sciencedirect.com/science/article/pii/S0957178725000530.

[26] ENTSO-E, "Electricity balancing in europe: An overview of the european balancing market and electricity balancing guideline," European Network of Transmission System Operators for Electricity, Nov. 2018, Accessed: 2026-03-23. [Online]. Available: https://www.entsoe.eu/

Documents/Network%20codes%20documents/NC%20EB/entso-e_balancing_in%20_europe_report_Nov2018_web.pdf.

[27] Nano Energies. "Frequency control reserve (fcr)." Accessed: 2026-03-23. [Online]. Available: https://nanoenergies.eu/knowledge-base/frequency-control-reserve-fcr.

[28] Svenska Kraftnät, "Ancillary services in power systems," Svenska Kraftnät, Sweden, Tech. Rep., 2025, Technical Report.

[29] ENTSO-E, "Frequency containment reserves (fcr) implementation framework," European Network of Transmission System Operators for Electricity, Brussels, Belgium, Tech. Rep., 2019, Technical Report.

[30] ENTSO-E, "Nordic synchronous area: Frequency stability and control," European Network of Transmission System Operators for Electricity, Brussels, Belgium, Tech. Rep., 2021, Technical Report.

[31] S. Engelken et al., "Inertial response in modern power systems," *IEEE Transactions on Power Systems*, pp. 1234–1245, 2017.

[32] W. Kempton and J. Tomić, "Vehicle-to-grid power fundamentals: Calculating capacity and net revenue," *Journal of Power Sources*, pp. 268–279, 2005.

[33] Svenska Kraftnät, "Frequency containment reserves (fcr) in the nordic power system," Svenska Kraftnät, Stockholm, Sweden, Tech. Rep., 2023, Technical Report.

[34] H. Berg, *Batteries for Electric Vehicles: Materials and Electrochemistry*. Cambridge University Press, 2015.

[35] N. Nasajpour-Esfahani et al., "Comprehensive review of lithium-ion battery materials and development challenges," *Renewable and Sustainable Energy Reviews*, p. 114 783, 2024, ISSN: 1364-0321. [Online]. Available: https://www.sciencedirect.com/science/article/pii/S1364032124005094.

[36] M. Alipour, C. Ziebert, F. V. Conte, and R. Kizilel, "A review on temperature-dependent electrochemical properties, aging, and performance of lithium-ion cells," *Batteries*, 2020, ISSN: 2313-0105. [Online]. Available: https://www.mdpi.com/2313-0105/6/3/35.

[37] S. Zhang, K. Xu, and T. Jow, "The low temperature performance of li-ion batteries," *Journal of Power Sources*, pp. 137–140, 2003, ISSN: 0378-7753. [Online]. Available: https://www.sciencedirect.com/science/article/pii/S0378775302006183.

[38] G. Yarimca and E. Cetkin, "Review of cell level battery (calendar and cycling) aging models: Electric vehicles," *Batteries*, 2024, ISSN: 2313-0105. [Online]. Available: https://www.mdpi.com/2313-0105/10/11/374.

[39] J. Zhang, H. Huang, G. Zhang, Z. Dai, Y. Wen, and L. Jiang, "Cycle life studies of lithium-ion power batteries for electric vehicles: A review," *Journal of Energy Storage*, p. 112 231, 2024, ISSN: 2352-152X. [Online]. Available: https://www.sciencedirect.com/science/article/pii/S2352152X24018176.

[40] M. A. Mohamed, T. F. Yu, G. Ramsden, J. Marco, and T. Grandjean, "Advancements in parameter estimation techniques for 1rc and 2rc equivalent circuit models of lithium-ion batteries: A comprehensive review," *Journal of Energy Storage*, p. 115 581, 2025, ISSN: 2352-152X. [Online]. Available: https://www.sciencedirect.com/science/article/pii/S2352152X25002944.

[41] A. Krupp, R. Beckmann, T. Diekmann, E. Ferg, F. Schuldt, and C. Agert, "Calendar aging model for lithium-ion batteries considering the influence of cell characterization," *Journal of Energy Storage*, p. 103 506, 2022, ISSN: 2352-152X. [Online]. Available: https://www.sciencedirect.com/science/article/pii/S2352152X21011889.

[42] X. Cui, F. Stroebl, M. Uppaluri, V. N. Lam, W. C. Chueh, and S. Onori, "Long-term calendar aging across commercial lithium-ion cell chemistries—modeling and early prediction," *Journal of The Electrochemical Society*, p. 060 521, 2025.

[43] J. Nájera, J. Arribas, R. de Castro, and C. Núñez, "Semi-empirical ageing model for lfp and nmc li-ion battery chemistries," *Journal of Energy Storage*, p. 108 016, 2023, ISSN: 2352-152X. [Online]. Available: https://www.sciencedirect.com/science/article/pii/S2352152X23014135.

[44] C. Amzallag, J. Gerey, J. Robert, and J. Bahuaud, "Standardization of the rainflow counting method for fatigue analysis," *International Journal of Fatigue*, pp. 287–293, 1994, ISSN: 0142-1123. [Online]. Available: https://www.sciencedirect.com/science/article/pii/0142112394903433.

[45] R. Khezri, D. Steen, E. Wikner, and L. A. Tuan, "Optimal v2g scheduling of an ev with calendar and cycle aging of battery: An milp approach," *IEEE Transactions on Transportation Electrification*, pp. 10 497–10 507, 2024.

[46] M. Matsuishi and T. Endo, "Fatigue of metals subjected to varying stress," *Proceedings of the Japan Society of Mechanical Engineers*, 1968, in Japanese; English summary presented 1974.

[47] S. D. Downing and D. F. Socie, "Simple rainflow counting algorithms," *International Journal of Fatigue*, pp. 31–40, 1982.

[48] ASTM International, "ASTM E1049-85(2017): Standard Practices for Cycle Counting in Fatigue Analysis," ASTM International, West Conshohocken, PA, Tech. Rep., 2017.

[49] K. Rumpf, M. Naumann, and A. Jossen, "Experimental investigation of parametric cell-to-cell variation and correlation based on 1100 commercial lithium-ion cells," *Journal of Energy Storage*, pp. 224–243, 2017, ISSN: 2352-152X. [Online]. Available: https://www.sciencedirect.com/science/article/pii/S2352152X17302633.

[50] M. Naumann, M. Schimpe, P. Keil, H. C. Hesse, and A. Jossen, "Analysis and modeling of calendar aging of a commercial lifepo4/graphite cell," *Journal of Energy Storage*, pp. 153–169, 2018, ISSN: 2352-152X. [Online]. Available: https://www.sciencedirect.com/science/article/pii/S2352152X18300665.

[51] M. Naumann, F. B. Spingler, and A. Jossen, "Analysis and modeling of cycle aging of a commercial lifepo4/graphite cell," *Journal of Energy Storage*, p. 227 666, 2020, ISSN: 0378-7753. [Online]. Available: https://www.sciencedirect.com/science/article/pii/S0378775319316593.

[52] A. Soto, A. Berrueta, M. Mateos, P. Sanchis, and A. Ursúa, "Impact of micro-cycles on the lifetime of lithium-ion batteries: An experimental study," *Journal of Energy Storage*, p. 105 343, 2022.

[53] P. Keil et al., "Calendar aging of lithium-ion batteries i. impact of the graphite anode on capacity fade," *Journal of The Electrochemical Society*, 2016. [Online]. Available: `https://api.semanticscholar.org/CorpusID:100297055`.